

See discussions, stats, and author profiles for this publication at: <https://www.researchgate.net/publication/236833028>

# Analysis of high-pressure hydrogen, methane, and heptane laminar diffusion flames: Thermal diffusion factor modeling

ARTICLE *in* COMBUSTION AND FLAME · JUNE 2007

Impact Factor: 3.08 · DOI: 10.1016/j.combustflame.2007.06.007

---

CITATIONS

21

---

READS

54

## 2 AUTHORS:



[Sridhar Palle](#)

Jackson State University

12 PUBLICATIONS 57 CITATIONS

[SEE PROFILE](#)



[Richard Steven Miller](#)

Clemson University

54 PUBLICATIONS 1,090 CITATIONS

[SEE PROFILE](#)



# Analysis of high-pressure hydrogen, methane, and heptane laminar diffusion flames: Thermal diffusion factor modeling

Sridhar Palle, Richard S. Miller \*

*Department of Mechanical Engineering, Clemson University, Clemson, SC 29634-0921, USA*

Received 26 October 2006; received in revised form 16 May 2007; accepted 15 June 2007

Available online 28 August 2007

## Abstract

Direct numerical simulations are conducted for one-dimensional laminar diffusion flames over a large range of pressures ( $1 \leq P_0 \leq 200$  atm) employing a detailed multicomponent transport model applicable to dense fluids. Reaction kinetics mechanisms including pressure dependencies and prior validations at both low and high pressures were selected and include a detailed 24-step, 12-species hydrogen mechanism ( $\text{H}_2/\text{O}_2$  and  $\text{H}_2/\text{air}$ ), and reduced mechanisms for methane ( $\text{CH}_4/\text{air}$ : 11 steps, 15 species) and heptane ( $\text{C}_7\text{H}_{16}/\text{air}$ : 13 steps, 17 species), all including thermal  $\text{NO}_x$  chemistry. The governing equations are the fully compressible Navier–Stokes equations, coupled with the Peng–Robinson real fluid equation of state. A generalized multicomponent diffusion model derived from nonequilibrium thermodynamics and fluctuation theory is employed and includes both heat and mass transport in the presence of concentration, temperature, and pressure gradients (i.e., Dufour and Soret diffusion). Previously tested high-pressure mixture property models are employed for the viscosity, heat capacity, thermal conductivity, and mass diffusivities. Five models for high-pressure thermal diffusion coefficients related to Soret and Dufour cross-diffusion are first compared with experimental data over a wide range of pressures. Laminar flame simulations are then conducted for each of the four flames over a large range of pressures for all thermal diffusion coefficient models and results are compared with purely Fickian and Fourier diffusion simulations. The results reveal a considerable range in the influence of cross-diffusion predicted by the various models; however, the most plausible models show significant cross-diffusion effects, including reductions in the peak flame temperatures and minor species concentrations for all flames. These effects increase with pressure for both  $\text{H}_2$  flames and for the  $\text{C}_7\text{H}_{16}$  flames indicating the elevated importance of proper cross-diffusion modeling at large pressures. Cross-diffusion effects, while not negligible, were observed to be less significant in the  $\text{CH}_4$  flames and to decrease with pressure. Deficiencies in the existing thermal diffusion coefficient models are discussed and future research directions suggested.

© 2007 The Combustion Institute. Published by Elsevier Inc. All rights reserved.

**Keywords:** Supercritical; High-pressure; Laminar diffusion flame; Soret diffusion; Dufour diffusion; Real gas; Hydrogen; Methane; Heptane; Multicomponent

---

\* Corresponding author. Fax: +1 864 656 4435.  
E-mail address: [rm@clemson.edu](mailto:rm@clemson.edu) (R.S. Miller).

## 1. Introduction

Multicomponent fluid mixing and combustion at high pressures is a subject receiving relatively recent scrutiny in the literature. This is despite the fact that practical combustion devices routinely operate at pressures near or higher than the thermodynamic critical point (or “critical locus” for a mixture) of relevant hydrocarbon fuels ( $\sim 15 < P_C < 30$  atm [1]). Note that despite some varying opinions in the literature, for the purposes of this study “supercritical” is defined as having either the temperature or pressure fixed above the critical point (critical locus for a mixture), since no phase change is possible in either case. For example, diesel fuel is injected at very high pressure into a pressurized cylinder  $\sim 25$  atm, which is then increased to  $\sim 60$  atm after ignition [2–6]. Aircraft gas turbine combustor chambers operate at pressures  $\sim 30$  atm and have been steadily increasing at a near-linear rate for the past 60 years [7]. Typical rocket engines burning hydrogen and oxygen routinely operate at pressures  $\sim 100$  atm and larger.

Supercritical reacting mixtures are characterized by an absence of latent heat and surface tension, “liquidlike” densities, potential real gas effects manifested by nonunity compressibility factors, and pressure dependencies of species properties and reaction kinetics. Multicomponent and differential diffusion effects can also be significant at high pressures for many practical fuels; particularly those involving species with significantly varying molecular weights [8,9]. In addition, the relative importance of Dufour and Soret “cross-diffusion,” by which thermal energy diffuses in the presence of concentration and/or pressure gradients, and mass diffuses in the presence of thermal and/or pressure gradients, respectively, are substantially enhanced under these conditions for many practical fuels (although the Dufour effects are generally found to be negligible). This occurs because the “thermal diffusion coefficient” (the fluid property related to Soret diffusion) generally increases with pressure, with maximal values near the critical locus of the mixture. Such molecular transport effects can be important for both nonpremixed and premixed laminar flames, as both involve substantial temperature and concentration gradients within the local flame zone. Differences in molecular transport models can result both in variations in observed diffusion rates, as well as in alterations to local flame curvature and strain rates [10]. Ignition characteristics in high-pressure heptane flames have also been shown to be affected both by the assumption of unity Lewis number and by the inclusion of Soret and Dufour cross-diffusion [11].

Relatively little research has been done regarding combustion simulations incorporating compre-

hensive multicomponent diffusion, including Soret and Dufour cross-diffusion. In addition, existing research is almost exclusively limited to kinetic-theory-based derivations for low-pressure systems [12]. Under low-pressure conditions, the generalized Stefan–Maxwell relations provide the most comprehensive means of predicting multicomponent diffusion incorporating cross-diffusion (e.g., Refs. [13–15]) and provide expressions for all of the associated transport properties. The formulation requires the solution of a coupled set of  $N \times N$  matrix equations for an  $N$ -species system requiring substantial computational time [16]. Other simplified models have also been addressed, including various forms of Fick’s law [17–19]. Despite the relatively widespread neglect of cross-diffusion in the combustion community, many studies including these effects find them to be of substantial importance to proper flame modeling even at low-pressure (for both “light” and “heavy” species and for soot) [20–26]. However, in spite of the prevalence of high-pressure combustion devices, very little research has been conducted in multicomponent combustion at large pressures, in part due to the inapplicability of the kinetic-theory-based models under these conditions.

For high-pressure flows outside of the range of validity of kinetic theory, the proper theory for formulating the molecular fluxes is nonequilibrium thermodynamics (NEQT) [27]. However, in contrast to the Stefan–Maxwell relations, NEQT does not provide expressions for the transport properties. The mixture viscosity, thermal conductivity, mass diffusion coefficients, and thermal diffusion coefficients must therefore be provided through additional theory or models. Bellan’s group at the Jet Propulsion Laboratory have conducted extensive research into high-pressure binary species mixing with heat and mass diffusion fluxes derived from NEQT and Keizer’s fluctuation theory [28–30]. Their derivation includes the potential for both heat and mass diffusion in the presence of temperature, pressure, and concentration gradients. Two forms of the “thermal diffusion factors” were identified (the Irving–Kirkwood and the Bearman–Kirkwood forms;  $\alpha_{JK}$  and  $\alpha_{BK}$ , respectively), which are related thermodynamically such that only one factor is specified independently for each species pair. The relationship between the thermal diffusion factors and the experimentally measured thermal diffusion coefficients is described below. Real gas effects were accounted for with the cubic Peng–Robinson equation of state due to its relative computational efficiency and the availability of a simple correction that can be used to substantially increase its accuracy [31].

Bellan and co-workers have studied several binary fluid mixing problems under the above described formulation, including supercritical droplet “vapor-

ization” for oxygen in hydrogen [32,33] and heptane in nitrogen [29]. Among many results, it was observed that the effective Lewis number in supercritical mixtures can be 2–40 times larger than its typical definition in high-pressure heptane “droplet” diffusion (even when cross-diffusion is negligible), and both forms increase with pressure [34]. The formulation was then extended to the direct numerical simulation (DNS) of temporally developing binary mixing layers for heptane/nitrogen [35,36] and hydrogen/oxygen [37] (see Refs. [38,39] for recent reviews). The authors found in their droplet studies that the best agreement with experimental observations was obtained when the Irving–Kirkwood form of the thermal diffusion factor was assumed to be a small constant for the heptane–nitrogen cases ( $\alpha_{IK} \approx 0.1$ ), or a small constant for the Bearman–Kirkwood form for the hydrogen–oxygen cases ( $\alpha_{BK} \approx 0.2$ ) [39]. Mixing layer simulations found that the results were not particularly sensitive to the actual value of the “small” constants chosen [35]. Miller later attempted to generalize these observations to arbitrary species pairs by adopting a molecular-weight-ratio-based correlation originally proposed by Curtis and Farrell [40] to specify  $\alpha_{IK}$ . DNS was conducted for binary mixing of various species pairs in supercritical, stationary, isotropic turbulence [41]. Soret induced deviations from purely Fickian induced scalar variance decay rates and conditional expected scalar statistics were found to increase with increasing molecular weight ratio [41,42]. The derivation was then extended to ternary species systems by Lou and Miller [43,44], allowing the consideration of simple nonexothermic reactions of the form  $A + B \rightarrow P$ . In addition to the relatively simple thermal diffusion modeling, the above studies also generally employed simplistic modeling for the remaining transport properties (e.g., constant or simplified viscosity, Schmidt number, and Prandtl number models).

Most recently, the ternary species formulation has been applied to the simulation of one-dimensional (1D), single-step, irreversible, exothermic, laminar diffusion flames at high pressure [8,9]. Realistic high-pressure mixture models for the viscosity, thermal conductivity, and mass diffusivities based on the principle of corresponding states were employed and validated with experimental data. A parametric study was conducted for three model flames as a function of the nondimensional Damkohler number, heat release parameter, “flame Reynolds number,” and ambient pressure. All simulations were performed twice: once including, and once neglecting, Soret and Dufour diffusion. Soret diffusion effects are apparent when species with nonequal molecular weights are involved in the reaction and result in reductions of the peak flame temperature  $\sim 175$  K for a  $H_2 + 1/2O_2 \rightarrow H_2O$  re-

action. In addition, it was shown that neglect of cross-diffusion leads to deviations in the predicted flame thicknesses (approximately 25%), with underpredictions for a hydrogen–oxygen system and overpredictions for a heavy hydrocarbon reaction. These effects were explained in detail through examinations of the individual heat and mass flux vectors as well as through associated thermodynamic properties. Nevertheless, results from these relatively simple ternary-species-model simulations based on an assumed generalization of the thermal-diffusion-factor model may not be indicative of true flame behavior, and further research is needed.

The objectives of the present study are to extend the application of the NEQT theory to more realistic 1D laminar flame simulations in order to assess the true impact and pressure dependence of multicomponent diffusion and thermal-diffusion-factor modeling. In particular, the multicomponent diffusion derivation is extended to systems of arbitrary numbers of species, allowing the incorporation of detailed and reduced kinetics mechanisms for multispecies combustion of  $H_2/O_2$ ,  $H_2/air$ ,  $CH_4/air$ , and  $C_7H_{16}/air$  (all including thermal  $NO_x$  chemistry). Realistic Arrhenius rate kinetics parameters and enthalpies of formation for real heat release are added, and high-pressure property models are retained. In addition, five different high-pressure thermal-diffusion-coefficient models are first compared with experimental data and then incorporated into DNS flame simulations. For the present purposes DNS refers to simulations in which all length and time scales (including acoustic) are completely resolved through high-order-accurate simulations lacking any numerical diffusion. The majority of these models come from the hydrocarbon reservoir literature and have not yet been applied to combustion processes. Each of the thermal-diffusion-coefficient-model predictions is compared with the purely Fickian/Fourier model to assess the impact of cross-diffusion. Uncertainties in the thermal diffusion coefficient models are discussed, and recommendations for future research are described.

## 2. Governing equations and approach

The mathematical formulation and the numerical approach employed for the present study are extensions of those used previously by our group, and several details not presented can be found in Refs. [8,9,41]. The general high-pressure-flow formulation is based on the compressible form of the continuity, momentum, total-energy (internal plus kinetic), and species-mass-fraction equations,

$$\frac{\partial \rho}{\partial t} + \frac{\partial}{\partial x_j} [\rho u_j] = 0, \quad (1)$$

$$\frac{\partial}{\partial t}(\rho u_i) + \frac{\partial}{\partial x_j}[\rho u_i u_j + P \delta_{ij} - \tau_{ij}] = 0, \quad (2)$$

$$\begin{aligned} \frac{\partial}{\partial t}(\rho e_t) + \frac{\partial}{\partial x_j} \left[ (\rho e_t + P) u_j - u_i \tau_{ij} + Q_{BK,j} \right. \\ \left. + \sum_{\alpha=1}^N \bar{H}_{,\alpha} \bar{J}_{j,\alpha} \right] = S_e, \end{aligned} \quad (3)$$

where  $u_i$  is the mixture velocity vector,  $\rho$  is the mixture density,  $P$  is the pressure,  $\delta_{ij}$  is the Kronecker delta function tensor,  $\tau_{ij}$  is the viscous stress tensor (assumed Newtonian),  $e_t$  is the total sensible specific energy,  $Q_{BK,j}$  is the heat flux vector in Bearman–Kirkwood (BK) form,  $\sum_{\alpha=1}^N (\bar{H}_{,\alpha} \bar{J}_{j,\alpha})$  is the enthalpy flux term,  $\bar{H}_{,\alpha}$  is the partial molar enthalpy of species  $\alpha$ ,  $\bar{J}_{j,\alpha}$  is the molar mass flux vector of species  $\alpha$  (mass and molar mass flux vectors are related through the relation  $J_{j,\alpha} = M_{\alpha} \bar{J}_{j,\alpha}$ , where  $M_{\alpha}$  is the molecular weight of species  $\alpha$ ), and  $S_e$  is the reaction source term for the energy equation. An alternative form of the heat flux vector termed the Irving–Kirkwood (IK) form absorbs the enthalpy flux term into the definition of the heat flux vector:  $Q_{IK,j} = Q_{BK,j} + \sum_{\alpha=1}^N \bar{H}_{,\alpha} \bar{J}_{j,\alpha}$ . Transport equations for each of the mass fractions of species  $\alpha$  ( $Y_{\alpha}$ ) are

$$\frac{\partial}{\partial t}(\rho Y_{\alpha}) + \frac{\partial}{\partial x_j}[\rho Y_{\alpha} u_j + J_{j,\alpha}] = S_{Y_{\alpha}}. \quad (4)$$

The individual species are identified by  $\alpha = 1, 2, \dots, N$ , where  $N$  is total number of species and  $S_{Y_{\alpha}}$  is the reaction source term for each species' transport equation. Real gas effects are included through the cubic Peng–Robinson equation of state [1]. Although many other examples of real gas state equations exist [1], the Peng–Robinson form is relatively simple to apply and is relatively accurate for conditions not too “near” the critical locus. Furthermore, if additional accuracy were required, a relatively simple correction has been published [31]. Details of the state equation and its mixing rules may be found in Refs. [9,41].

### 2.1. Heat and mass flux vectors

General multicomponent forms of the heat and mass flux vectors derived from NEQT [27] and fluctuation theory [28] have been presented previously by Harstad and Bellan [29] for systems consisting of arbitrary numbers of species. The fluxes were re-derived for the present study (see Ref. [9] for the derivation) and are presented in an alternate form distinguishing terms proportional to gradients of temperature ( $T$ ), mole fraction ( $X$ ), and pressure ( $P$ ):  $Q_{BK,j} = Q_{BK,j}^T + Q_{BK,j}^{X_1} + \dots + Q_{BK,j}^{X_{\alpha=N-1}} + Q_{BK,j}^P$ ,

and  $J_{j,\alpha} = J_{j,\alpha}^T + J_{j,\alpha}^{X_1} + \dots + J_{j,\alpha}^{X_{\alpha=N-1}} + J_{j,\alpha}^P$  (subscript  $j$  denotes the vector component and  $\alpha$  denotes the species, and the superscripts indicate the thermodynamic gradient):

$$\begin{aligned} Q_{BK,j} = - \left\{ \kappa \right. \\ \left. + \sum_{\alpha=1}^{N-1} \sum_{\beta>\alpha}^N X_{\alpha} X_{\beta} \alpha_{BK}^{\alpha\beta} \frac{\bar{R}\rho}{M_m} D_m^{\alpha\beta} \right\} \frac{\partial T}{\partial x_j} \\ - \sum_{\alpha=1}^N \left\{ X_{\alpha} \sum_{\beta \neq \alpha}^N \left[ \frac{M_{\beta}}{M_m^2} X_{\beta} \alpha_{BK}^{\alpha\beta} \rho D_m^{\alpha\beta} \right] \bar{V}_{,\alpha} \right\} \frac{\partial P}{\partial x_j} \\ - \sum_{\gamma=1}^{N-1} \sum_{\alpha=1}^N \left\{ \bar{R}T \sum_{\beta \neq \alpha}^N \left[ \frac{M_{\beta}}{M_m^2} X_{\beta} \alpha_{BK}^{\alpha\beta} \rho D_m^{\alpha\beta} \right] \alpha_D^{\alpha\gamma} \right\} \\ \times \frac{\partial X_{\gamma}}{\partial x_j}, \end{aligned} \quad (5)$$

$$\begin{aligned} \bar{J}_{j,\alpha} = - \sum_{\beta \neq \alpha}^N n D_m^{\alpha\beta} \left\{ \frac{X_{\alpha} X_{\beta}}{T} \frac{M_{\beta}}{M_m} \alpha_{BK}^{\alpha\beta} \right\} \frac{\partial T}{\partial x_j} \\ - \sum_{\beta \neq \alpha}^N \frac{n D_m^{\alpha\beta}}{\bar{R}T} \left\{ - \frac{M_{\alpha} M_{\beta}}{M_m^2} X_{\alpha} X_{\beta} \bar{V}_{,\beta} \right. \\ \left. + \frac{M_{\alpha} M_{\alpha}}{M_m^2} X_{\alpha} X_{\beta} \bar{V}_{,\alpha} \right\} \frac{\partial P}{\partial x_j} \\ - \sum_{\gamma=1}^{N-1} \left\{ \sum_{\beta \neq \alpha}^N \left[ - \frac{M_{\alpha} M_{\beta}}{M_m^2} X_{\alpha} n D_m^{\alpha\beta} \alpha_D^{\beta\gamma} \right. \right. \\ \left. \left. + \frac{M_{\beta} M_{\beta}}{M_m^2} X_{\beta} n D_m^{\beta\alpha} \alpha_D^{\alpha\gamma} \right] \right\} \frac{\partial X_{\gamma}}{\partial x_j}. \end{aligned} \quad (6)$$

The alternative IK form of the heat flux vector is

$$\begin{aligned} Q_{IK,j} \\ = - \left\{ \kappa + \sum_{\alpha=1}^{N-1} \sum_{l>\alpha}^N X_{\alpha} X_l \alpha_{IK}^{\alpha\beta} \alpha_{BK}^{\alpha\beta} \frac{\bar{R}\rho}{M_m} D_m^{\alpha\beta} \right\} \frac{\partial T}{\partial x_j} \\ - \sum_{\alpha=1}^N \left\{ X_{\alpha} \sum_{l \neq \alpha}^N \left[ \frac{M_l}{M_m^2} X_l \alpha_{IK}^{\alpha\beta} \rho D_m^{\alpha\beta} \right] \bar{V}_{,\alpha} \right\} \frac{\partial P}{\partial x_j} \\ - \sum_{\gamma=1}^{N-1} \sum_{\alpha=1}^N \left\{ \bar{R}T \sum_{l \neq \alpha}^N \left[ \frac{M_l}{M_m^2} X_l \alpha_{IK}^{\alpha\beta} \rho D_m^{\alpha\beta} \right] \alpha_D^{\alpha\gamma} \right\} \\ \times \frac{\partial X_{\gamma}}{\partial x_j} \end{aligned} \quad (7)$$

(no implied summations over repeated Greek indices). In the above,  $n$  is the molar density ( $n = \rho/M_m$ ), the mixture molecular weight is  $M_m = \sum_{\alpha=1}^N X_{\alpha} M_{\alpha}$ , the universal gas constant is  $\bar{R}$ , and the partial molar volume of species  $\alpha$  is  $\bar{V}_{,\alpha}$ .



Several properties appear in the above: the mixture thermal conductivity is  $\kappa$ , the “mass diffusivities” within the mixture are  $D_m^{\alpha\beta}$  for species pair  $\alpha, \beta$ , and the “mass diffusion factor” pairs are  $\alpha_D^{\alpha\beta}$ , which can in theory be derived from the chosen equation of state. Finally, two forms of the dimensionless “thermal diffusion factor” pairs appear in the above, the BK and the IK forms:  $\alpha_{BK}^{\alpha\beta}$ , and  $\alpha_{IK}^{\alpha\beta}$ , respectively. These two factors are directly related to the relative extent of cross-diffusion in the system and are related thermodynamically [29],

$$\alpha_{IK}^{\alpha\beta} = \alpha_{BK}^{\alpha\beta} + \frac{1}{RT} \frac{M_\alpha M_\beta}{M_m} \left( \frac{\bar{H}_{,\alpha}}{M_\alpha} - \frac{\bar{H}_{,\beta}}{M_\beta} \right), \quad (8)$$

where  $\bar{H}_{,\alpha}$  is the partial molar enthalpy of species  $\alpha$ , and  $\alpha_{IK}^{\alpha\beta} = -\alpha_{IK}^{\beta\alpha}$  and  $\alpha_{BK}^{\alpha\beta} = -\alpha_{BK}^{\beta\alpha}$ . Thus, only one factor needs to be specified as a property of the particular species pair, the other being determined by thermodynamics from the choice of equation of state. However, if the heat flux vector is written in the BK form ( $Q_{BK,j}$ ), then only  $\alpha_{BK}^{\alpha\beta}$  appears in the formulation. Forms of the partial molar volumes, the partial molar enthalpies, and the heat capacity departure functions derived from the Peng–Robinson state equation have appeared previously (e.g., Refs. [9,41]). In addition to the above, the “mass diffusion coefficient” is defined as the product of the mass diffusivity and the mass diffusion factor ( $D_m \alpha_D$ ) and the “thermal diffusion coefficient” is defined as the ratio of the thermal diffusion factor to the mass diffusion factor ( $\alpha_{BK} / \alpha_D$ ). These are the quantities typically measured in (binary species) experiments. The “coefficients” therefore implicitly include mass diffusion factor effects (their distinction is discussed further below).

Several of the results to follow are based on the multicomponent Fourier and Fickian forms of the flux vectors, i.e., neglecting cross-diffusion. Fourier’s heat conduction law is reduced from the BK heat flux vector by nulling all  $\alpha_{BK}^{\alpha\beta}$ , resulting in  $Q_{BK,j} = -\kappa \partial T / \partial x_j$ . The multicomponent Fickian diffusion flux form is obtained by also nulling the thermal diffusion factors and neglecting terms proportional to pressure gradients:

$$\bar{J}_{j,\alpha} = - \sum_{\gamma=1}^{N-1} \left\{ \sum_{\beta \neq \alpha}^N \left[ - \frac{M_\alpha M_\beta}{M_m^2} X_\alpha n D_m^{\alpha\beta} \alpha_D^{\beta\gamma} + \frac{M_\beta M_\beta}{M_m^2} X_\beta n D_m^{\beta\alpha} \alpha_D^{\alpha\gamma} \right] \right\} \frac{\partial X_\gamma}{\partial x_j}. \quad (9)$$

A more simplified form often considered in combustion studies [18] is based on an effective diffusion coefficient (again implicitly including mass diffusion factor effects) assuming diffusion of species  $\alpha$  is only

due to the species’ own mole or mass fraction gradient:  $J_{j,\alpha} = -\rho D_m^{\alpha,\text{eff}} \partial Y_\alpha / \partial x_j$ . Various models exist for calculating  $D_m^{\alpha,\text{eff}}$  in terms of the actual species diffusivities, including the popular Wilke rule [45]; however, “naive” application of the Wilke formula does not ensure that the summation of all mass flux vectors is null. This naive application has been shown to result in errors as large as 70% in evaluating the mass flux vectors [17]. Therefore, several corrections to this approach have been proposed such as defining the flux vector of the  $N$ th species to be  $J_{j,N} = -\sum_{\alpha=1}^{N-1} J_{j,\alpha}$  or through the addition of terms to the flux formulation [46]. However, only the complete multicomponent form is considered in this study, in order to isolate the effects of cross-diffusion (see for example Ref. [17] for a comparison of the various simpler forms of the Fickian mass flux vector).

## 2.2. Property modeling

Closure of the above sets of governing equations requires the specification of the low-pressure reference heat capacities ( $C_{p,0}$ ), mixture viscosity ( $\mu$ ), mixture thermal conductivity ( $\kappa$ ), mass diffusivities ( $D_m^{\alpha\beta}$ ), mass diffusion factors ( $\alpha_D^{\alpha\beta}$ ), and thermal diffusion factors ( $\alpha_{IK}^{\alpha\beta}$  or  $\alpha_{BK}^{\alpha\beta}$ ) for all species (pairs) in the system. Low-pressure, temperature-dependent, reference heat capacity correlations have been obtained through the NIST Webbook (as well as data for comparisons) [47]. In order to generalize the approach, models consistent with the principle of corresponding states have been chosen when possible. The models implemented for the mixture viscosity, thermal conductivity, heat capacities, and mass diffusivities and comparisons with experimental data have appeared previously [8]. For species in which deviations exist, the departures have been curve fitted and added as corrections to the models. Additional details, including all species critical properties, acentric factors, atomic diffusion volumes, and enthalpies of formation, are provided in Ref. [9]. The mass diffusion factors are thermodynamic functions related to molar gradients of the fugacity coefficients. They approach unity at low pressures, recovering the standard Fickian form of the mass flux vector, but can deviate substantially from unity near the critical locus of the mixture (where the mass diffusion factors approach zero, leading to vanishing mass diffusion coefficients and infinite thermal diffusion coefficients). The derivation of the mass diffusion factors from the state equation is quite complex and its evaluation is known to be quite sensitive to the form of the state equation as well as to the mixing rules employed. However, for conditions not too near the critical locus, ideal mixing may be assumed. In this case, the Gibbs–

Duhem relation yields  $\alpha_D^{\alpha\beta} = 1$  for  $\alpha = \beta$ ,  $\alpha_D^{\alpha\beta} = 0$  for  $\alpha \neq \beta$ , and  $\alpha_D^{\alpha\beta} = -1$  for  $\alpha = N$ . The approach taken in the present study is to assume ideal mixing in conjunction with the mass diffusivities, but to implicitly include (potential) nonideal mass diffusion factors with respect to the thermal diffusion coefficients (as described below).

Many issues remain to be addressed in regard to high-pressure, multicomponent mass diffusivity, and mass diffusion factor modeling. The majority of experimental techniques available are generally limited to measuring near-infinite-dilution mass diffusion coefficients for binary species systems ( $\alpha_D$  is unity at the mole fraction boundary). Relatively little is known about proper mass diffusivity or mass coefficient modeling for general molar composition mixtures, even for the binary case under these conditions. Less is known concerning mixtures with more than two species present. For the present purposes the rates of mass diffusion are modeled using existing high-pressure binary species diffusion coefficient models together with the (unity) ideal-mixing mass diffusion factor model. Problems associated with this assumption are inherent in all multicomponent combustion models employing realistic properties and are not the focus of the current paper. In fact, these issues are alleviated in the current work, as the focus is on determining the change in flame properties imparted by including Soret and Dufour diffusion vs not including cross diffusion, with all other effects held constant. Furthermore, the flame temperatures in the results presented below are much higher than the critical values for any of the constituent mixture species, providing justification for the present ideal mixing model usage.

The emphasis of the current work is on the impact of cross-diffusion in realistic laminar diffusion flames as a function of pressure. However, cross-diffusion is directly related to the specification of the thermal diffusion factor pairs (either the BK or IK forms related through Eq. (8)), which are relatively poorly understood, particularly at large pressures for which kinetic-theory-based derivations are inapplicable. Nevertheless, several models have been proposed and experimental data [48,49] exist with which to evaluate the performance of the models under high-pressure conditions. For example, Shukla and Firoozabadi [50] compared predictions of several models for the Bearman–Kirkwood form of the thermal diffusion coefficient with binary species data up to pressures as high as 200 atm. The models tested were generally in qualitative agreement with the data trends. However, those models which agreed reasonably well for hydrocarbon/hydrocarbon species pairs typically performed relatively poorly for hydrocarbon/nonhydrocarbon species pairs, and vice versa. In addition, the majority

of available models require derivations of thermodynamic quantities from the chosen equation of state. They are known to be considerably sensitive to both the choice of the equation of state as well as to the particular mixing rules applied [51]. Data and models for thermal diffusion factors in larger than binary species systems are much more sparse and are generally limited to ternary species systems [52,53]. Therefore, only binary species forms of the thermal diffusion factor models are considered in this work. It is assumed that the mixture interaction parameters  $\alpha_{BK}^{\alpha\beta}$  can be modeled using binary species models modified for use in multicomponent mixtures where appropriate. Although the thermal diffusion of a species *A* into a species *B* will be altered by the presence of other mixture species, the theoretical description of thermal diffusion in large numbers of species (and data with which to test the models) is relatively immature at this point. The approach is consistent with the treatment of the mixture mass diffusion coefficients nearly universally adopted in the literature as well as in the present study, which are also poorly understood for multicomponent mixtures.

Several of the models and comparisons with experimental data found in the hydrocarbon reservoir literature [50] are repeated for convenience in what follows. Two forms of a model previously applied in high-pressure droplet, mixing, and combustion studies are also included. Kinetic theory is not applicable under the conditions of interest to this study and is therefore not included in what follows. The five models for the thermal diffusion factor pairs evaluated are the “Hasse model” (denoted HM) [54], the “Kempers model” (denoted KM) [55], the “Shukla and Firoozabadi model” (denoted FM) [50], and two variations of a model proposed by Curtis and Farrell (denoted CM1 and CM2) [40]. The first three models are based on semitheoretical/empirical derivations as functions of partial molar volume, partial molar enthalpy, and/or partial molar internal energy differences among species pairs (the reader is referred to the original citations for details of the derivations and modeling assumptions). For the present investigation these are calculated from the Peng–Robinson equation of state [9]. The models are presented below in the forms applied to the current multicomponent formulation. It is noted that these models and the experimental measurements to be presented below actually apply to the thermal diffusion coefficient defined previously. However, for the present purposes these models are employed for the thermal diffusion factors ( $\alpha_{BK}^{\alpha\beta}$ ) directly and in conjunction with the (unity) ideal mixing model for the mass diffusion factors. In this case potential departures from unity mass diffusion factors are implicitly included through the various models for the thermal diffusion coefficients,

although the factors are kept distinct in the formulation. For conditions of unity mass diffusion factor, the thermal diffusion factor and the thermal diffusion coefficient are equivalent (as are the mass diffusivity and the mass diffusion coefficient). Note, however, that the model implementation would have to be modified if a nonideal model for the mass diffusion factors were considered. The last model is a molecular-weight-ratio-based correlation fit to experimental data but implicitly is a function of partial molar enthalpy differences in one of the forms tested.

Hasse [54] proposed a model for evaluating the thermal diffusion coefficient in binary mixtures based on irreversible thermodynamics,

$$\alpha_{\text{BK}}^{\alpha\beta} = \frac{M_\alpha(\bar{H}_{,\beta} - \bar{H}_{,\beta}^0) - M_\beta(\bar{H}_{,\alpha} - \bar{H}_{,\alpha}^0)}{M_m X_\alpha \left(\frac{\partial \mu_\alpha}{\partial X_\alpha}\right)_{T,P,n}} + \frac{\alpha_T^0 \bar{R}T}{X_\alpha \left(\frac{\partial \mu_\alpha}{\partial X_\alpha}\right)_{T,P,n}}, \quad (10)$$

where  $\mu_\alpha$  is the chemical potential of species  $\alpha$ . The model is based on the departure of the partial molar enthalpy from its pure ideal gas limit (superscript 0). In the above,  $\alpha_T^0$  is the thermal diffusion coefficient at the standard state (ideal gas) and can be calculated from the kinetic theory of gases. However, it has been previously observed (Refs. [50,56]) that the contribution of  $\alpha_T^0$  is negligible at large pressures, and an alternate “modified Hasse model” form is recommended in which  $\alpha_T^0$  is taken to be zero in the above. This modified form is adopted for the present study (implications are discussed below).

Kempers [55] proposed a model for estimating the binary thermal diffusion coefficient which is also based on phenomenological theory. Unlike the Hasse model (HM), the Kempers model (KM) requires the standard state partial molar enthalpies ( $\bar{H}_\alpha^0$ : pure ideal gas state for species  $\alpha$ )

$$\alpha_{\text{BK}}^{\alpha\beta} = \frac{\bar{V}_{,\alpha} \bar{H}_{,\beta} - \bar{V}_{,\beta} \bar{H}_{,\alpha}}{\bar{V}_m X_\alpha \left(\frac{\partial \mu_\alpha}{\partial X_\alpha}\right)_{T,P,n}}. \quad (11)$$

Application of the model is limited to liquids and dense gases.

Shukla and Firoozabadhi [50] proposed a model for predicting binary thermal diffusion coefficients, also based on the thermodynamics of irreversible processes,

$$\alpha_{\text{BK}}^{\alpha\beta} = \left[ \frac{(\bar{U}_{,\alpha}/\tau_\alpha - \bar{U}_{,\beta}/\tau_\beta)}{X_\alpha (\partial \mu_\alpha / \partial X_\alpha)_{T,P}} + \frac{(\bar{V}_{,\beta} - \bar{V}_{,\alpha}) \sum_{\gamma=1}^N (X_\gamma \bar{U}_{,\gamma} / \tau_\gamma)}{\bar{V}_m X_\alpha \left(\frac{\partial \mu_\alpha}{\partial X_\alpha}\right)_{T,P}} \right], \quad (12)$$

where  $\bar{U}_{,\alpha}$  is the partial molar internal energy of species  $\alpha$ . The above model (denoted as FM) requires the values of  $\tau_\alpha$  for species  $\alpha$ , which can in theory be determined from viscosity data according to Ref. [50]. However, Shukla and Firoozabadhi [50] recommend using a constant value for all  $\tau_\alpha = 4$ . This approach has been adopted in the current work.

The final two models considered are based on a molecular-weight-based correlation originally proposed by Curtis and Farrell [40] in high-pressure droplet vaporization studies. Two forms of the model are considered, based on using the correlation to predict either the IK or BK form of the thermal diffusion factor pairs (denoted models CM1 and CM2, respectively),

$$\alpha_{\text{IK}}^{\alpha\beta}, \alpha_{\text{BK}}^{\alpha\beta} = 2.3842 \times 10^{-2} + (0.24821) \log_{10} \left( \frac{M_\alpha}{M_\beta} \right), \quad (13)$$

where  $\alpha$  is the species with the high molecular weight. Although applied to high-pressure conditions, the correlation is based on atmospheric pressure data and does not include pressure or temperature dependence in its original form specifying  $\alpha_{\text{BK}}^{\alpha\beta}$ . The values predicted are relatively small ( $\sim 10^{-1}$ ) and inconsistent with much larger values typically measured for high-pressure fluids (see below). It is, however, consistent with Bellan's recommendation of  $\alpha_{\text{BK}} = 0.2$  for high-pressure  $\text{H}_2/\text{O}_2$  [39] (the model predicts  $\approx 0.32$ ) and will be evaluated below as model CM2. In contrast, model CM1 uses the above correlation to specify  $\alpha_{\text{IK}}$ . The BK form,  $\alpha_{\text{BK}}$ , is then obtained through Eq. (8), implicitly bringing in temperature and pressure dependence through the partial molar enthalpies. This form has been used in Refs. [8,41,42,44] and was originally based on Bellan's recommendation of  $\alpha_{\text{IK}} = 0.1$  for high-pressure heptane/nitrogen droplet vaporization after comparisons with experimental droplet data (the model predicts  $\approx 0.16$ ) in order to generalize the formulation to additional species pairs. Comparisons with experimental data are presented below for each of the five thermal diffusion factor models.

### 2.3. Chemical kinetics mechanisms

Three different complete chemical kinetics mechanisms have been added to the DNS code, and 1D laminar diffusion flames for each case have been extensively documented in Ref. [9] for pressures in the range  $1 \rightarrow 200$  atm. Although more “standard” mechanisms exist in some cases, only mechanisms with pressure-dependent reaction pathways and prior validations with high-pressure data were considered.



Table 1

Detailed chemical kinetic mechanism for H<sub>2</sub>/air combustion [57] and corresponding forward reaction constants:  $k_r = AT^\beta \times \exp(-E_A/\bar{R}T)$

| No. | Reaction                                      | A [cm mol s]          | $\beta$ | $E_a$ [kJ/mol] |
|-----|---|-----------------------|---------|----------------|
| 1   | $O_2 + H \rightleftharpoons OH + O$           | $2.00 \times 10^{14}$ | 0.00    | 70.30          |
| 2   | $H_2 + O \rightleftharpoons OH + H$           | $5.06 \times 10^4$    | 2.67    | 26.30          |
| 3   | $H_2 + OH \rightleftharpoons H_2O + H$        | $1.00 \times 10^8$    | 1.60    | 13.8           |
| 4   | $OH + OH \rightleftharpoons H_2O + O$         | $1.50 \times 10^9$    | 1.14    | 0.42           |
| 5   | $H + H + M \rightleftharpoons H_2 + M$        | $1.80 \times 10^{18}$ | -1.00   | 0.00           |
| 6   | $H + OH + M \rightleftharpoons H_2O + M$      | $2.20 \times 10^{22}$ | -2.00   | 0.00           |
| 7   | $O + O + M \rightleftharpoons O_2 + M$        | $2.90 \times 10^{17}$ | -1.00   | 0.00           |
| 8   | $H + O_2 + M \rightleftharpoons HO_2 + M$     | $2.30 \times 10^{18}$ | -0.80   | 0.00           |
|     | $k_\infty$                                    | $4.52 \times 10^{13}$ | 0.00    | 0.00           |
| 9   | $HO_2 + H \rightleftharpoons OH + OH$         | $1.50 \times 10^{14}$ | 0.00    | 4.20           |
| 10  | $HO_2 + H \rightleftharpoons H_2 + O_2$       | $2.50 \times 10^{13}$ | 0.00    | 2.90           |
| 11  | $HO_2 + H \rightleftharpoons H_2O + O$        | $3.00 \times 10^{13}$ | 0.00    | 7.20           |
| 12  | $HO_2 + O \rightleftharpoons OH + O_2$        | $1.80 \times 10^{13}$ | 0.00    | -1.70          |
| 13  | $HO_2 + OH \rightleftharpoons H_2O + O_2$     | $6.00 \times 10^{13}$ | 0.00    | 0.00           |
| 14  | $HO_2 + HO_2 \rightleftharpoons H_2O_2 + O_2$ | $2.50 \times 10^{11}$ | 0.00    | -5.20          |
| 15  | $OH + OH + M \rightleftharpoons H_2O_2 + M$   | $3.25 \times 10^{22}$ | -2.00   | 0.00           |
|     | $k_\infty$                                    | $7.45 \times 10^{13}$ | -0.37   | 0.00           |
| 16  | $H_2O_2 + H \rightleftharpoons H_2 + HO_2$    | $1.70 \times 10^{12}$ | 0.00    | 15.70          |
| 17  | $H_2O_2 + H \rightleftharpoons H_2O + OH$     | $1.00 \times 10^{13}$ | 0.00    | 15.00          |
| 18  | $H_2O_2 + O \rightleftharpoons OH + HO_2$     | $2.80 \times 10^{13}$ | 0.00    | 26.80          |
| 19  | $H_2O_2 + OH \rightleftharpoons H_2O + HO_2$  | $5.40 \times 10^{12}$ | 0.00    | 4.20           |
| 20  | $O + N_2 \rightleftharpoons N + NO$           | $1.90 \times 10^{14}$ | 0.00    | 319.03         |
| 21  | $N + O_2 \rightleftharpoons O + NO$           | $1.13 \times 10^{10}$ | 1.00    | 27.83          |
| 22  | $N + OH \rightleftharpoons H + NO$            | $4.79 \times 10^{13}$ | 0.00    | 5.23           |
| 23  | $NO + HO_2 \rightleftharpoons NO_2 + OH$      | $3.00 \times 10^{12}$ | 0.00    | 10.04          |
| 24  | $NO + OH \rightleftharpoons NO_2 + H$         | $5.90 \times 10^{12}$ | 0.00    | 129.49         |

Note. Third body efficiencies: H<sub>2</sub> = 1.00, O<sub>2</sub> = 0.35, H<sub>2</sub>O = 6.5, N<sub>2</sub> = 0.4. Reaction rate coefficients dependent on pressure are calculated as  $k_r = k_\infty k_0[M]/(k_\infty + k_0[M])$ , where  $k_0$ , and  $k_\infty$  are the low- and high-pressure reaction rate coefficients, respectively.

A detailed 24-step, 12-species mechanism applicable to both H<sub>2</sub>/O<sub>2</sub> and H<sub>2</sub>/air combustion by Sohn et al. [57], including 5-step NO<sub>x</sub> chemistry [58], is employed. Reduced mechanisms for two different hydrocarbon fuels (methane and heptane) have been chosen, based on their relevance to many practical combustion applications. For the CH<sub>4</sub> oxidation, an 11-step, 15-species reduced mechanism by Hewson and Bolig [59] is used, while a 13-step, 17-species reduced mechanism by Bolig et al. [60] is employed for heptane (C<sub>7</sub>H<sub>16</sub>) oxidation; both including 6-step NO<sub>x</sub> chemistry [59]. The three mechanisms are presented in Tables 1–3, respectively. Backward reaction rates for the detailed hydrogen mechanism, and all details concerning the evaluation of reaction rates, reaction constants, and steady state species relations for the two reduced mechanisms are provided in Ref. [9].

#### 2.4. Numerical approach

The present study examines molecular transport effects in 1D laminar diffusion flames. Although 1D

Table 2

Reduced chemical kinetics mechanism for CH<sub>4</sub>/air combustion

| No. | Reaction   |
|-----|--|
| 1   | $CH_4 + 2H + H_2O \rightleftharpoons CO + 4H_2$          |
| 2   | $CO + H_2O \rightleftharpoons CO_2 + H_2$                |
| 3   | $2H \rightleftharpoons H_2$                              |
| 4   | $3H_2 + O_2 \rightleftharpoons 2H + 2H_2O$               |
| 5   | $2CO + H_2 \rightleftharpoons C_2H_2 + O_2$              |
| 6   | $N_2 + O_2 \rightleftharpoons 2NO$                       |
| 7   | $3H_2 + CO + NO \rightleftharpoons HCN + H + 2H_2O$      |
| 8   | $NO + CO + H + H_2O \rightleftharpoons HNCO + O_2 + H_2$ |
| 9   | $NH_3 + H + H_2O \rightleftharpoons NO + 3H_2$           |
| 10  | $N_2 + H_2O \rightleftharpoons N_2O + H_2$               |
| 11  | $NO + 2H_2 + O_2 \rightleftharpoons NO_2 + H_2O + 2H$    |

Note. See Ref. [9] for all reaction constant specifications and steady species relations.

similarity solutions for strained flames are often considered, the similarity transforms applied to the 2D strained flame problem do not exist for the general compressible flow equations currently consid-

Table 3  
Reduced chemical kinetics mechanism for C<sub>7</sub>H<sub>16</sub>/air

| No. | Reaction   |
|-----|--|
| 1   | $3\text{H}_2 + \text{O}_2 \rightleftharpoons 2\text{H} + 2\text{H}_2\text{O}$                                    |
| 2   | $2\text{H} \rightleftharpoons \text{H}_2$  |
| 3   | $\text{CO} + \text{H}_2\text{O} \rightleftharpoons \text{CO}_2 + \text{H}_2$                                     |
| 4   | $\text{C}_2\text{H}_2 + 2\text{H}_2\text{O} + 2\text{H} \rightleftharpoons 2\text{CO} + 4\text{H}_2$             |
| 5   | $\text{C}_2\text{H}_4 \rightleftharpoons \text{C}_2\text{H}_2 + \text{H}_2$                                      |
| 6   | $\text{C}_3\text{H}_6 \rightleftharpoons 1.5\text{C}_2\text{H}_4$  |
| 7   | $\text{C}_7\text{H}_{16} \rightleftharpoons \text{C}_3\text{H}_6 + 2\text{C}_2\text{H}_4 + \text{H}_2$           |
| 8   | $\text{N}_2 + \text{O}_2 \rightleftharpoons 2\text{NO}$  |
| 9   | $3\text{H}_2 + \text{CO} + \text{NO} \rightleftharpoons \text{HCN} + \text{H} + 2\text{H}_2\text{O}$             |
| 10  | $\text{NO} + \text{CO} + \text{H} + \text{H}_2\text{O} \rightleftharpoons \text{HNCO} + \text{O}_2 + \text{H}_2$ |
| 11  | $\text{NH}_3 + \text{H} + \text{H}_2\text{O} \rightleftharpoons \text{NO} + 3\text{H}_2$                         |
| 12  | $\text{N}_2 + \text{H}_2\text{O} \rightleftharpoons \text{N}_2\text{O} + \text{H}_2$                             |
| 13  | $\text{NO} + 2\text{H}_2 + \text{O}_2 \rightleftharpoons \text{NO}_2 + \text{H}_2\text{O} + 2\text{H}$           |

Note. See Ref. [9] for all reaction constant specifications and steady species relations.

ered. Therefore, unstrained laminar flames are simulated following the approach of Ref. [8]. In summary, the unsteady governing equations are solved on a simple one-dimensional domain,  $-L_2/2 \leq x_2 \leq L_2/2$ , where  $L_2$  is the total domain length. A fourth-order Runge–Kutta explicit time-marching scheme is employed for all time derivatives, coupled with eighth-order accurate (nondissipative) central finite differencing for all spatial derivatives (with tenth-order accurate explicit filtering to control numerical oscillations) [61]. Nonreflecting outflow boundary conditions are applied at  $x_2 = \pm L_2/2$  [62] and the Fortran code is parallelized using the MPI subroutines. Error function profiles are used to specify all species' initial conditions, including an overlap of fuel and oxidizer used both to initiate the reactions and to provide resolvable gradients in the initial conditions. The error function,  $\eta = \text{erf}(\pi^{1/2}x_2/\delta_0)$ , defines the physical overlap thickness  $\delta_0$ , which must be sufficiently small to ensure adequate resolution of all molecular length scales without numerical diffusion. In practice, a “flame Reynolds number” ( $\text{Re}_F = \rho_0 a_0, \delta_0/\mu_0$ ) is defined for convenience based on the average density, acoustic velocity, and viscosity of the two free streams for each flame considered. For each simulation the overlap thickness is determined by taking the same value,  $\text{Re}_F = 1000$ , for consistency, and a sufficient spatial (and temporal) resolution is determined through grid (and time step) refinement for each case. This includes a complete resolution of all reaction, diffusion, and acoustic scales. In practice, 2000 grid points are used for the majority of the simulations, with a viscous Courant number of 0.1 (the long time flame zone covers  $\sim 1/10$  of the total number of grid points). The total domain length varied with the initial overlap thickness and with the particular simulation requirements and varied in the range

$14.58\delta_0 \geq L_2 \geq 87.48\delta_0$ . Details of the initial species profiles are described below.

The nature of DNS with its relatively small Reynolds number restrictions makes direct comparisons with high-pressure experimental flows intractable. The code verification and validation has therefore been conducted as follows: All of the “mandatory” numerical checks for conservation of mass and energy, nonnegative mass fractions, grid resolution and time step independence, etc., have been made. The basic DNS code engine was the basis for all of our prior published studies in this area and has also been tested in the past by reproducing published simulation data for (low-pressure) isotropic turbulence and mixing layers. As mentioned above, each of the chemical kinetics mechanisms was compared with both low- and high-pressure data in their original citations. Although the 1D laminar diffusion flame in our simulations is not an exact match for the (typically strained-flame) geometries in the original citations, all of our predicted species concentrations and flame temperatures are in good agreement with the published data. The real gas state equation has been tested extensively through comparisons with a variety of experimental fluid density data both at Clemson and in Ref. [31] across the range of thermodynamic regimes of interest. All property models employed in the code have undergone extensive comparisons with available high-pressure data for a variety of substances. Property data were generally obtained through the NIST Webbook [47] and Ref. [63]. Model comparisons for the viscosity, thermal conductivity, mass diffusivity, and constant-pressure heat capacity have been published in Refs. [8,9] and show excellent agreement over the range 1–100 atm for all species tested. Comparisons of the thermal diffusion coefficient models with high-pressure experimental data as well as reproduction of published model evaluations are provided below. At each stage of the code's advancement, its consistency with previous results has been thoroughly tested (i.e., ensuring that the ternary species code reproduces the binary species results, the arbitrary species form reproduces ternary and binary species results, etc.).

### 3. Results

The results of the present study are presented in two stages. First, comparisons of each of the five thermal diffusion coefficient models with high-pressure experimental data are presented. This is followed by a documentation of 1D laminar flame simulations for each of the four flames described above. Each flame simulation is repeated with each of the five thermal diffusion coefficient models presented above, as well

as the purely Fickian and Fourier forms for comparison.

### 3.1. Thermal diffusion coefficient model evaluations

Figs. 1–3 present each of the five thermal diffusion coefficient models predictions for a variety of binary species pairs as a function of pressure, temperature, and concentration, respectively. The experimental data are all taken from Ref. [50] (original citations provided therein). Only the BK form of the thermal diffusion coefficient is presented, since this is the only form that appears explicitly in the formulation

when the BK form of the heat flux vector is used (the IK form appears due to the inclusion of the enthalpy fluxes in the definition of the IK form of the heat flux vector and is not directly related to cross-diffusion). The present results are in excellent agreement with those presented in Ref. [50] for the HM, FM, and KM models, in which the Peng–Robinson state equation was also used (deviations for some species data were attributed to sensitivity to the particular choice of mixing rules). The species pairs considered include  $\text{CH}_4/\text{C}_3\text{H}_8$ ,  $\text{CH}_4/\text{C}_4\text{H}_{10}$ ,  $\text{C}_7\text{H}_{16}/\text{C}_{12}\text{H}_{26}$ ,  $\text{N}_2/\text{CO}_2$ ,  $\text{H}_2/\text{N}_2$ ,  $\text{H}_2/\text{CO}_2$ ,  $\text{CH}_4/\text{N}_2$ , and  $\text{CH}_4/\text{CO}_2$ . One trend readily apparent in the experimental data is that the

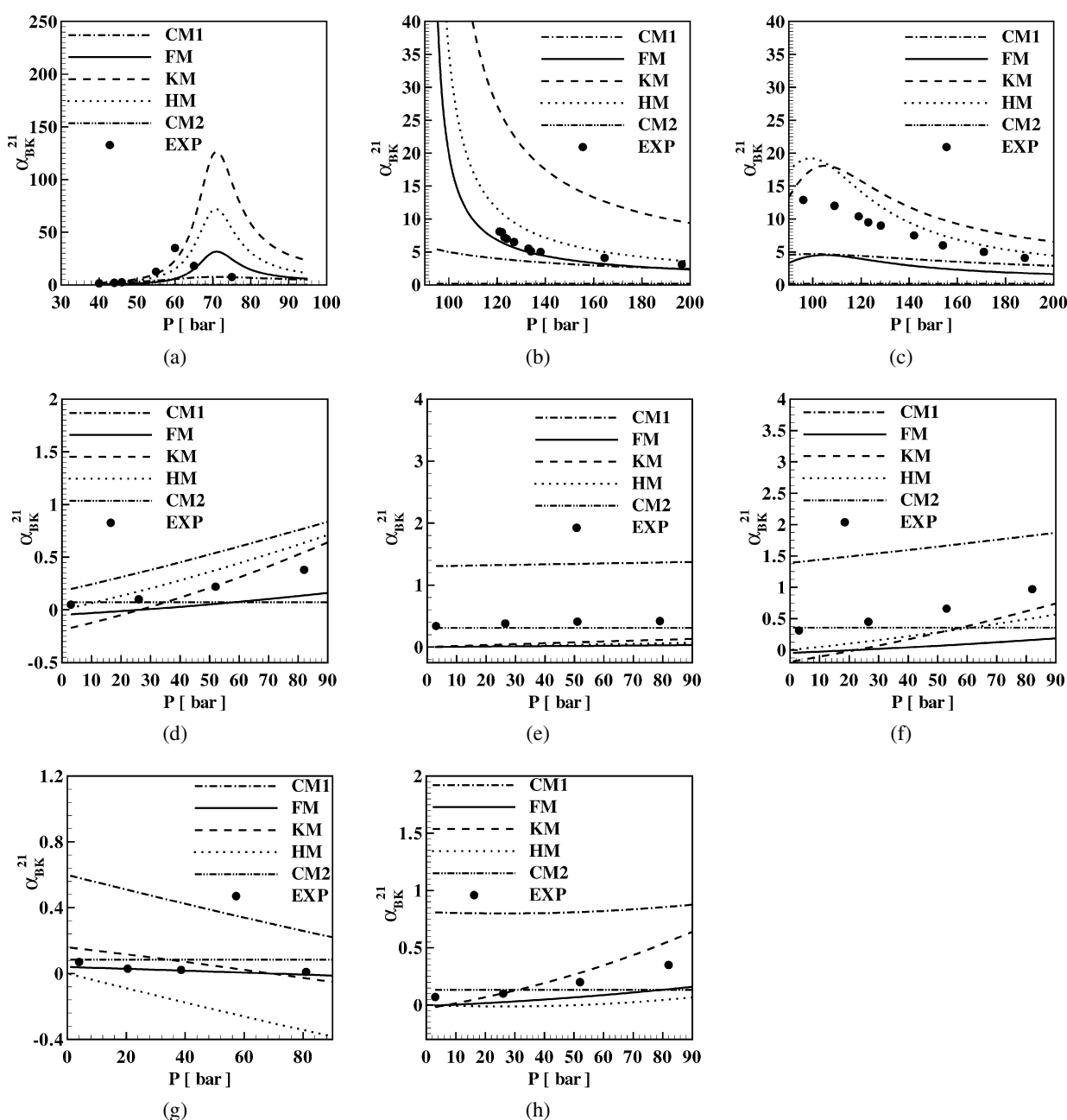


Fig. 1. Comparison of binary thermal diffusion coefficients evaluated by different models and experimental data as a function of pressure for (a)  $\text{CH}_4/\text{C}_3\text{H}_8$  at  $T = 346$  K,  $X_{\text{CH}_4} = 0.34$ , (b)  $\text{CH}_4/\text{C}_4\text{H}_{10}$  at  $T = 344$  K,  $X_{\text{CH}_4} = 0.49$ , (c)  $\text{CH}_4/\text{C}_4\text{H}_{10}$  at  $T = 394$  K,  $X_{\text{CH}_4} = 0.49$ , (d)  $\text{N}_2/\text{CO}_2$  at  $T = 357$  K,  $X_{\text{N}_2} = 0.52$ , (e)  $\text{H}_2/\text{N}_2$  at  $T = 357$  K,  $X_{\text{H}_2} = 0.5$ , (f)  $\text{H}_2/\text{CO}_2$  at  $T = 357$  K,  $X_{\text{H}_2} = 0.5$ , (g)  $\text{CH}_4/\text{N}_2$  at  $T = 357$  K,  $X_{\text{CH}_4} = 0.5$ , and (h)  $\text{CH}_4/\text{CO}_2$  at  $T = 357$  K,  $X_{\text{CH}_4} = 0.52$ .

thermal diffusion coefficients generally increase substantially (by as much as two orders of magnitude) from their low-pressure values as the pressure increases toward the critical locus (Fig. 1a). Somewhere near the molar average of the species' pair critical pressures, further increases in pressure again reduce the thermal diffusion coefficients (see, e.g., Figs. 1a–1c). However, for temperatures high with respect to the species critical temperatures, the peak is no longer apparent and a near-linear variation with pressure is observed (Figs. 1d–1h). The coefficients also vary significantly with concentration, indicating that even isothermal and isobaric mixing simulations will require nonconstant values (Fig. 3). One limitation of the data is that only relatively low temperatures are covered ( $295 < T < 395$  K), as the original studies were generally related to the petroleum reservoir field. The authors are not aware of any high-pressure and high-temperature data with which to more thoroughly test the models under the actual flame conditions of interest (discussed further below).

Several conclusions may be drawn regarding the performance of the various models. First, no single model is capable of accurately predicting both the qualitative and quantitative values of the thermal diffusion coefficients for all of the species pairs. Nevertheless, several of the models perform reasonably well; particularly considering that considerable uncertainty exists in the experimental data as well. Model CM2, which assumes a constant “small” value for  $\alpha_{BK}$  via a correlation to low-pressure data, is entirely inconsistent with the high-pressure data. All of the models incorrectly predict the pressure at which the maximum  $\alpha_{BK}$  value is found for  $\text{CH}_4/\text{C}_3\text{H}_8$  in Fig. 1a (although the location of the maximum is sensitive to the choice of mixing rules used in the underlying state equation). The models also behave differently for hydrocarbon/hydrocarbon species pairs (Figs. 1a–1c) than for nonhydrocarbon/nonhydrocarbon (Figs. 1d–1f), and hydrocarbon/nonhydrocarbon pairs (Figs. 1g and 1h). For example, model CM1 underpredicts the data in the first case, yet consistently overpredicts the data in the latter two cases. The HM and FM models appear to agree most reasonably with a wide range of data; however, both can predict inconsistent signs (negative values) for  $\alpha_{BK}$  under some conditions (see Figs. 1g and 2a, respectively). This would manifest itself in a reversal in the direction of the Soret diffusion flux.

One limitation of the present analysis is the fact that the experimental data are limited to low temperatures considerably below the conditions found in flames. Several of the models will be shown below to have unexpected and, most likely, unphysical behavior at large temperatures in the flame zone. Therefore, more accurate modeling work remains neces-

sary and experimental data at both high-pressures and high temperatures is needed for model validations. This may not be possible for pertinent species, as chemical reactions will commence at high temperatures relevant to combustion, making measurements of either mass or thermal diffusion coefficients either extremely difficult or impossible. Nevertheless, arguments can be made concerning expected trends at high temperatures and the range of models considered generally encompass the available data in all cases. The forthcoming simulations of laminar diffusion flames using these models should, therefore, put bounds on the extent of Soret and Dufour cross-diffusion that would be expected from any improved models.

### 3.2. Flame simulations

Each of the five thermal diffusion coefficient models (applied to the thermal diffusion factors in conjunction with the ideal mixing model for the mass diffusion factors as described previously) is next assessed for its effects on the four 1D laminar flame simulations described above ( $\text{H}_2/\text{O}_2$ ,  $\text{H}_2/\text{air}$ ,  $\text{CH}_4/\text{air}$ , and  $\text{C}_7\text{H}_{16}/\text{air}$ ). Each simulation is repeated with purely Fickian/Fourier (multicomponent) diffusion model as well in order to measure the relative effects of the cross-diffusion predicted by the various models. The results will focus on the  $\text{H}_2/\text{air}$  flame first, followed by related results for the remaining flames. The transient flame simulations are sensitive to the initial species profiles chosen and therefore the effects of the initial conditions are addressed first. For the sake of simplicity and to ensure that all low-pressure cases are for gas phase fuels (phase change not being in the model), the initial temperature field for all simulations is constant with  $T_0 = 700$  K. The pressure field is also initially uniform at  $P_0$ , and the velocity is initially null. All initial species profiles are based on the error function provided above. At the ambient temperature considered, many of the reaction mechanisms will not result in ignition without the initialization of various radical species. In fact, the simulation results are highly sensitive to the level of radical initialization chosen, which can result in maximum flame temperatures varying by hundreds of degrees. Therefore, a variety of initial conditions were simulated for each flame. As will be demonstrated, the relative extent to which the various thermal diffusion factor models affected the flame variables is relatively insensitive to the initial conditions; thereby allowing general conclusions to be made from data for specific initial conditions.

#### 3.2.1. $\text{H}_2/\text{air}$ flames

For each flame simulation, a minimum of three different sets of initial species profiles were simu-



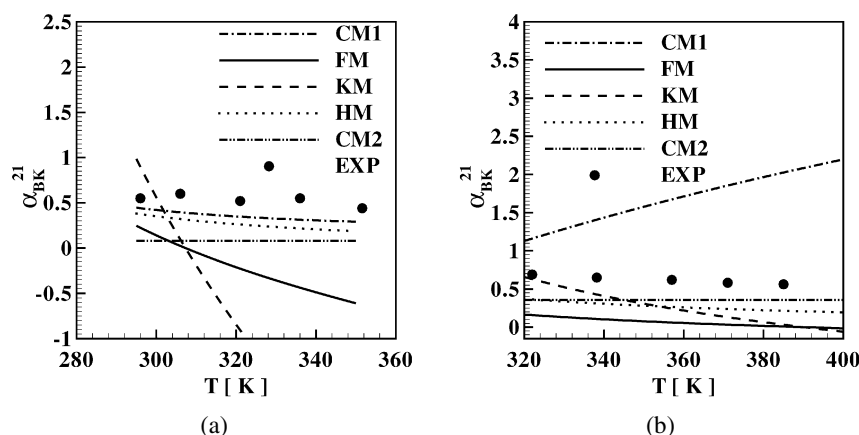


Fig. 2. Comparison of binary thermal diffusion coefficients evaluated by different models and experimental data as a function of temperature for (a)  $C_7H_{16}/C_{12}H_{26}$  at  $P = 1.01325$  bar,  $X_{C_7H_{16}} = 0.5$  and (b)  $H_2/CO_2$  at  $P = 49$  bar,  $X_{H_2} = 0.52$ .

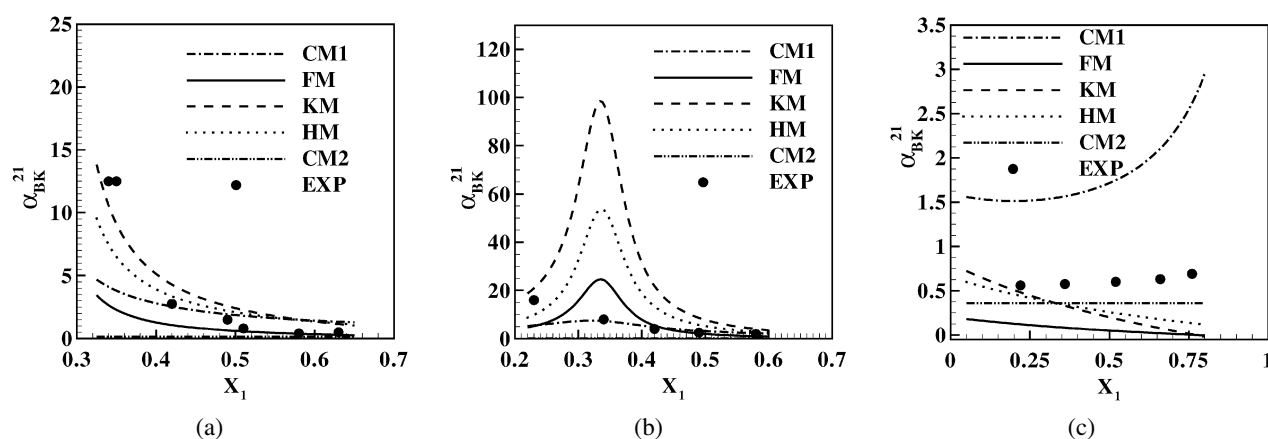


Fig. 3. Comparison of binary thermal diffusion coefficients evaluated by different models and experimental data as a function of mole fraction (of the first listed species) for (a)  $CH_4/C_3H_8$  at  $T = 346$  K,  $P = 55$  bar, (b)  $CH_4/C_3H_8$  at  $T = 346$  K,  $P = 75$  bar, (c)  $H_2/CO_2$  at  $T = 363$  K,  $P = 48$  bar.

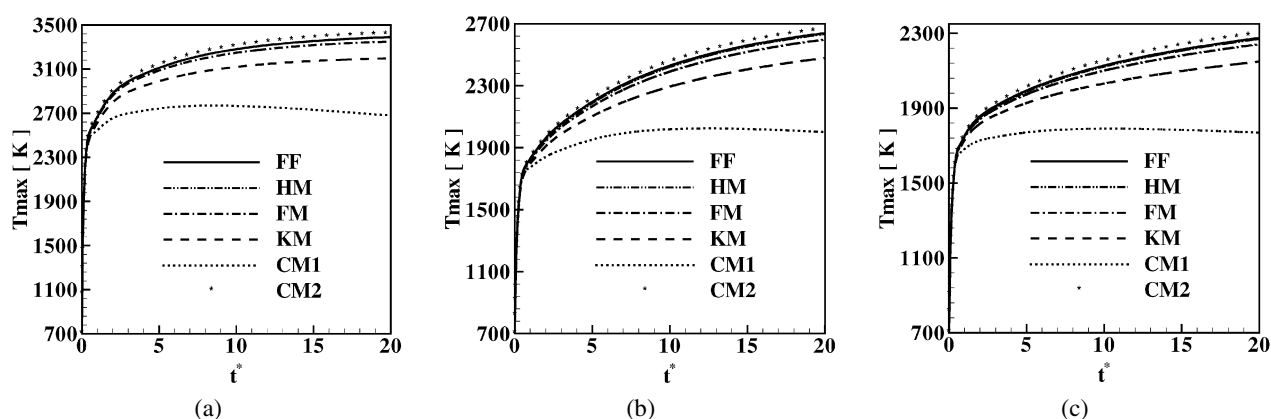


Fig. 4. Maximum flame temperature evolution for the base case ( $T_0 = 700$  K,  $P_0 = 100$  atm)  $H_2$ /air flame for various thermal diffusion factor models: initial conditions (a) IC1, (b) IC2, and (c) IC3.

lated. Considering first the detailed  $H_2$ /air mechanism, three initial conditions were chosen by varying the relative level of radical species within the initial fuel/oxidizer overlap region as follows. Base case results are first discussed in detail for an ambient pressure of  $P_0 = 100$  atm. All initial conditions have pure  $H_2$  in the  $x_2 < 0$ , and pure air ( $N_2$  plus  $O_2$ ) in the

$x_2 > 0$  free streams, respectively. An initial condition designated “IC1” has minimal mass fractions of ( $\sim 0.01$ ) for OH, O,  $H_2O$ ,  $HO_2$ , and  $H_2O_2$  initialized along with the  $H$  radical with a maximum mass fraction of 0.075 at the centerline. Initial condition “IC2” has the same  $H$  initialization, but the remaining subspecies mass fractions are initially null. Finally,

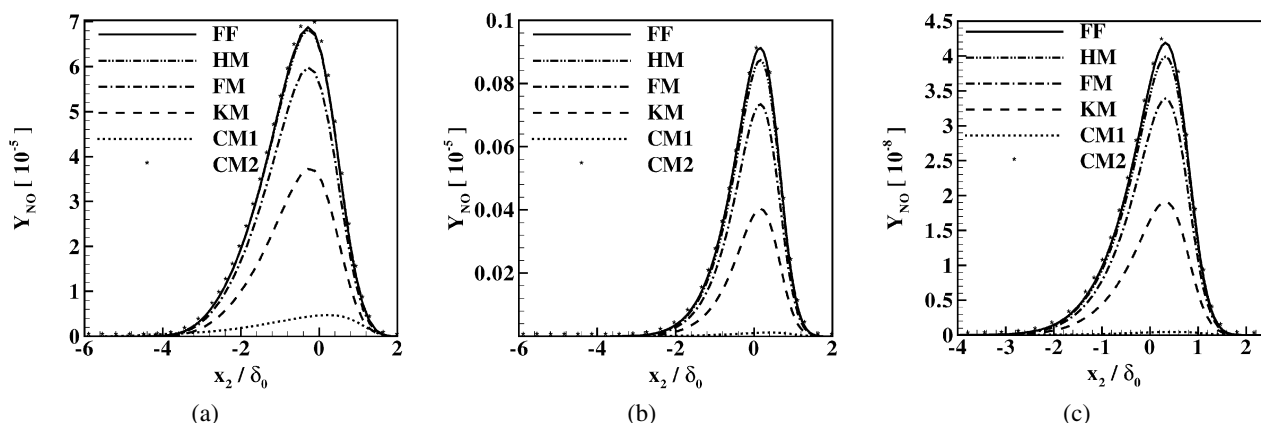


Fig. 5. Final time ( $t^* = 20$ ) NO mass fraction profiles for the base case ( $T_0 = 700$  K,  $P_0 = 100$  atm)  $H_2$ /air flame for various thermal diffusion factor models: initial conditions (a) IC1, (b) IC2, and (c) IC3.

“IC3” is the same as “IC2” but with a larger H mass fraction with a maximum of 0.1 (details provided in Ref. [9]). Initialization of radical species precludes the need for a numerical “spark plug” and the reactions proceed rapidly with relatively large heat release at initial times, adjusting to a quasi-steady state. It is noted that the IC3 case has an extremely large initial radical level. This is done intentionally in order to gauge the influence of initial conditions on the results.

Maximum flame temperature evolutions as predicted by the different cross-diffusion models and also by the standard Fourier/Fickian model (FF) have been plotted as a function of the nondimensional time variable  $t^* = t a_0 / \delta_0$  in Fig. 4 for the three sets of initial species profiles (IC1, IC2, and IC3). The maximum flame temperature is clearly sensitive to the choice of initial conditions, varying from approximately 2300 to 3500 K. However, the trends predicted by the cross-diffusion models in comparison to the purely Fickian/Fourier model are approximately equal for all of the initial conditions. In all cases, the Shukla and Firoozabadhi model (FM), the Kempers model (KM), and the Curtis and Farrell model 1 (CM1) result in lower maximum flame temperatures in comparison to the Fourier/Fickian model (FF). In contrast to the first two models, the CM1 model results in particularly large reductions in the flame temperature which decreases with time by the end of the simulations. The Hasse model (HM) has negligible influence on the maximum flame temperature and is similar to the Fourier/Fickian model. The Curtis and Farrell model 2 (CM2; constant thermal diffusion factors) predicts a very small increase in maximum flame temperature compared to the standard diffusion model (FF). Primary and subspecies mass fraction profiles are also affected by the choice of thermal diffusion factor model; however, the relative effects are essentially unaltered by the choice of initial conditions. For example, Fig. 5 presents the long-time NO mass fraction profiles at  $t^* = 20$  for each initial condition and each

thermal diffusion factor model. In this case even more dramatic reductions in peak mass fraction profiles are found for simulations including cross-diffusion (with the exception of model CM2). In fact, model CM1 results in essentially negligible NO production for each initial condition.

One important consequence of the above discussion is that the relative effects of the cross-diffusion modeling are essentially insensitive to the choice of initial conditions. Therefore, for the sake of convenience, only results for a single set of initial conditions (IC1) will be discussed in what follows. The long-time mass fraction profiles for several other species corresponding to IC1 are provided in Fig. 6. Similar trends are observed for each of the profiles, with model CM1 always resulting in the largest deviations from the FF model. The observed trends with respect to the various models can be explained in terms of their predicted thermal diffusion factor values. Figs. 1–3 compared the various binary thermal diffusion factor (coefficient) model predictions with experimental data. From these figures it was concluded that model CM2, which predicts constant  $\alpha_{BK}$  values, is inconsistent with observed trends and is a poor model. However, model CM1 appeared to predict the data reasonably well and generally with values bounded by the remaining model predictions. This would appear to be counter to the trends observed in the flame simulation for which model CM1 predicts the largest deviations from Fourier/Fickian behavior. In order to understand this apparent contradiction, it must be recalled that the data in Figs. 1–3 were all for relatively low temperatures in the range  $295 < T < 395$  K. In contrast, the mixing regions within the flame zone (where temperature and concentration gradients exist), where cross-diffusion will occur, are at much higher-temperatures. Understanding the high-temperature behavior of the various models is therefore crucial to deciphering the flame simulation results.

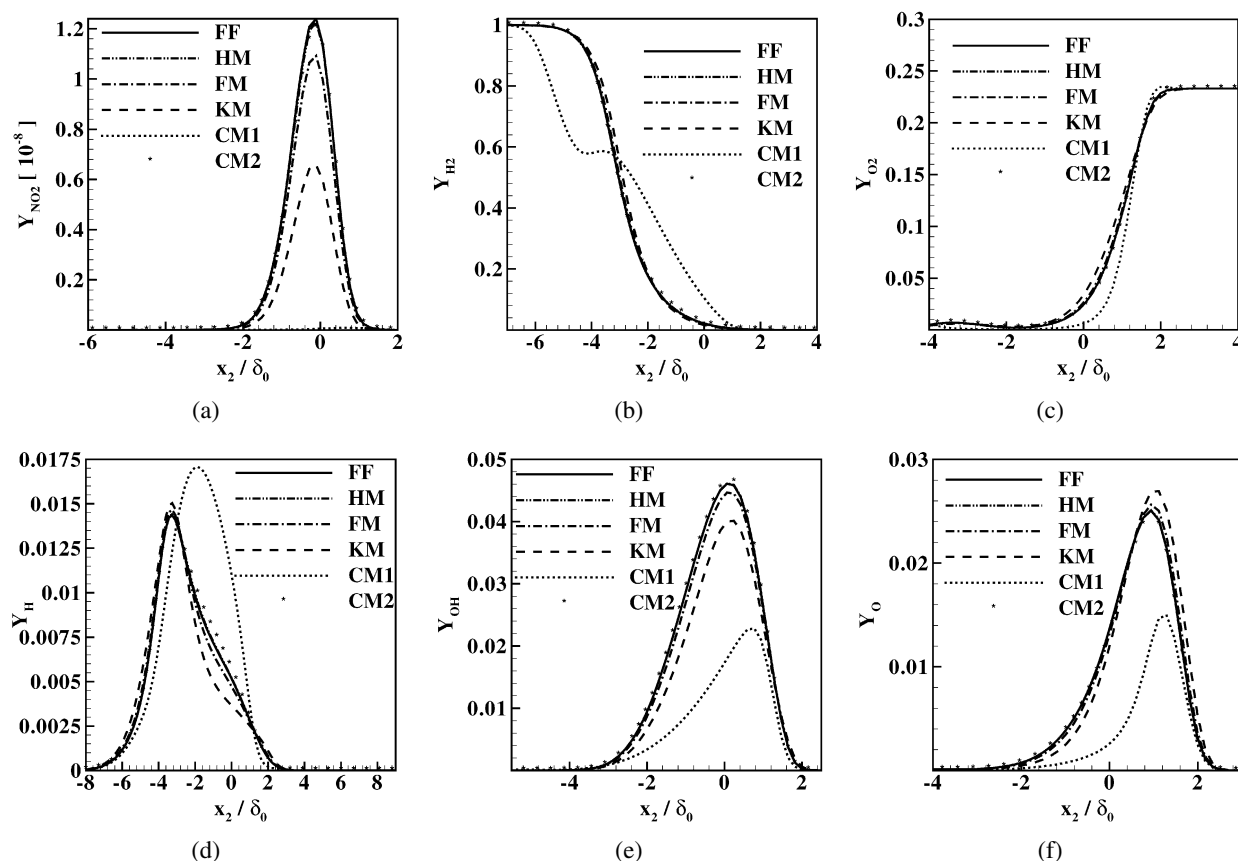


Fig. 6. Final time ( $t^* = 20$ ) mass fraction profiles for the base case ( $T_0 = 700$  K,  $P_0 = 100$  atm, initial condition IC1)  $H_2$ /air flame for various thermal diffusion factor models: (a)  $NO_2$ , (b)  $H_2$ , (c)  $O_2$ , (d)  $H$ , (e)  $OH$ , and (f)  $O$ .

For each flame simulation with  $N$  species there are  $(N^2 - N)/2$  independent thermal diffusion factors (since  $\alpha_{BK}^{\alpha\beta} = -\alpha_{BK}^{\beta\alpha}$  and the diagonal elements,  $\alpha_{BK}^{\alpha\alpha}$ , are null). Space constraints would therefore not allow a complete presentation of all of the possible thermal diffusion factor combinations for the multicomponent flames considered in this study. However, the analysis can be summarized with the aid of Fig. 7, which presents the various  $\alpha_{BK}^{21}$  model predictions for binary species systems having equal mass fractions for  $H_2/O_2$ ,  $CH_4/O_2$ , and  $C_7H_{16}/O_2$  (in order of species 1/2) as a function of pressure at a typical flame temperature of 2000 K. At these high temperatures all species pairs are far from their critical locus and relatively minimal pressure dependence is observed (see Fig. 1a in contrast). Model CM1 is in reasonable agreement with the remaining models for species pairs of comparable molecular weights ( $CH_4/O_2$  and  $C_7H_{16}/O_2$  in Figs. 7b and 7c, respectively). However, when the ratio of molecular weights is large, as for  $H_2/O_2$ , model CM1 predicts values nearly two orders of magnitude larger than the other models at high temperatures. Diffusion of  $H_2$  with  $O_2$  is obviously of great importance to the nonpremixed  $H_2/O_2$  and  $H_2$ /air flames, resulting in the observed amplified Soret effects. In contrast, for the  $CH_4$ /air and  $C_7H_{16}$ /air flames the mass fraction gradients of

$H_2$  are much less and a more consistent prediction is made by the CM1 model for these flames (see below).

Trends in the remaining models can also be observed. For example, the Hasse model (HM) shows nearly negligible Soret effects for all the flames ( $H_2/O_2$ ,  $CH_4$ /air, and  $C_7H_{16}$ /air are discussed below). In fact, the HM model predicts nearly null thermal diffusion factors for all species pairs at large temperatures (see Fig. 7). The reason for this is that the HM model is based on departures between the species partial molar enthalpies with their ideal gas limits (see Eq. (10)). As the temperatures become large the mixtures approach ideal gas behavior and the HM model predicts no Soret diffusion. This appears to be a deficiency in the model as Soret effects are known to be significant in many ideal gas mixtures (see citations above). It may be noted that only the “modified Hasse” model is currently considered, which neglects the (low-pressure) kinetic theory limiting behavior of the model. However, no significant deviations in the flame simulation results would be expected had this term been retained, because the kinetic theory values are approximately the same as those predicted by model CM2, which also predicts negligible Soret effects. Furthermore, there is little justification for believing that kinetic theory be the limiting behavior of high-temperature dense fluid sys-

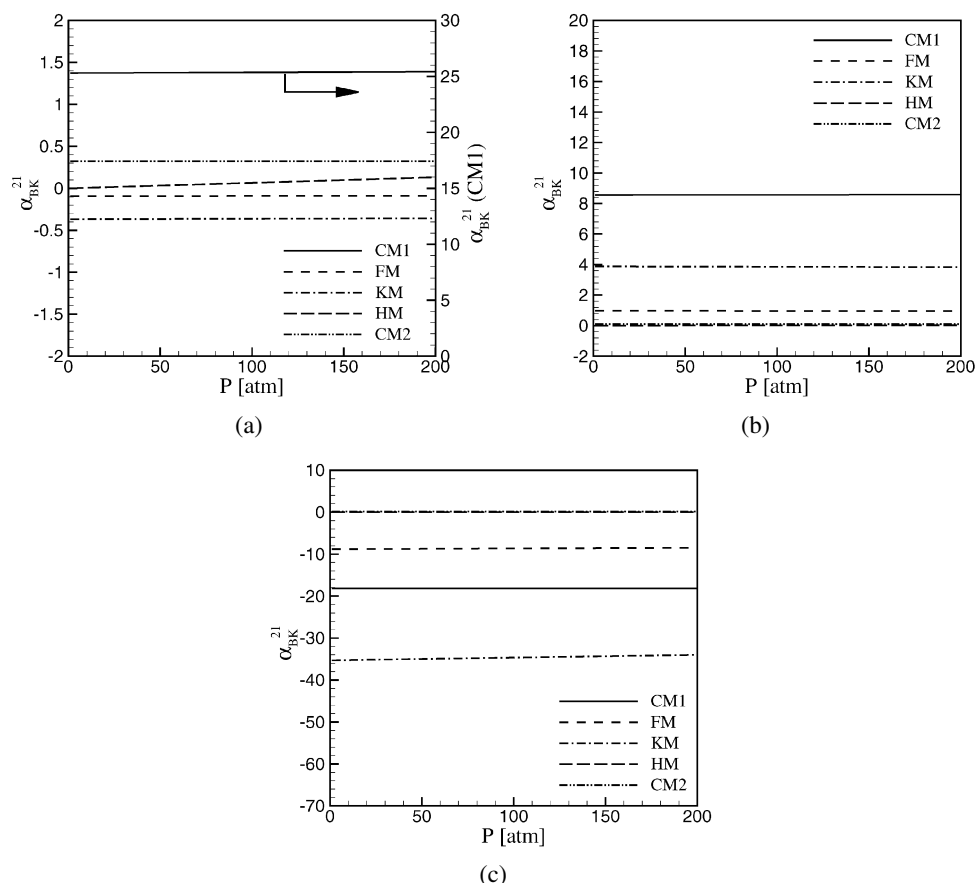


Fig. 7. High-temperature (2000 K) thermal diffusion factor model predictions for binary species pairs ( $Y_1 = Y_2 = 0.5$ ) as a function of pressure: (a)  $H_2/O_2$ , (b)  $CH_4/O_2$ , and (c)  $C_7H_{16}/O_2$ .

tems at the large pressures of interest to the study. This leaves the FM and KM models as the potentially most physically plausible models. Of the two, the FM model generally predicts the more conservative thermal diffusion factor values and may be recommended as the “safest” model due to its conservative estimates. However, before more conclusive evaluations of the various models can be made experimental data at both high pressures and high temperatures consistent with realistic combustion conditions are required. No such data is presently known to the authors.

Fig. 8 presents the long time heat and mass flux vector profiles predicted by both the FM and KM thermal diffusion factor models in the base case  $H_2$ /air flame. The Bearman–Kirkwood form of the heat flux vector is presented, and only the mass flux vectors corresponding to  $O_2$  and  $H_2$  are shown for the sake of brevity. In each case, the total flux vectors are presented along with those components proportional to temperature and pressure gradients, as well as the sum of all terms related to mole fraction gradients. As shown above, the KM model predicts larger values of the thermal diffusion factors and therefore exhibits enhanced cross-diffusion effects. Dufour diffusion is essentially negligible for the FM model (Fig. 8a) but is somewhat significant for the KM model (Fig. 8b). Soret diffusion slightly enhances the rate of  $O_2$  diffu-

sion into the flame zone, but decreases the rate of  $H_2$  diffusion. These effects are essentially negligible for the FM model (Figs. 8c and 8e) but are again more apparent for the KM model (Figs. 8d and 8f). Soret diffusion results in an approximately 15% reduction in the maximum mass flux rate of  $H_2$  into the flame zone (Fig. 8f). These results for mass fluxes only reveal a partial description of the complex multicomponent diffusion process which involves many species including radicals. The ultimate effects are apparent in the previously described species mass fraction profiles and maximum temperature evolutions.

### 3.2.2. $CH_4$ /air and $C_7H_{16}$ /air flames

Attention is now turned to the effects of cross-diffusion on the two flames described by reduced mechanisms:  $CH_4$ /air and  $C_7H_{16}$ /air. Fig. 9 depicts the maximum flame temperature evolution for each flame under base case conditions:  $T_0 = 700$  K, and  $P_0 = 35$  atm. Cross-diffusion effects are nearly negligible for all thermal-diffusion-factor models for the methane flame; whereas reductions in the long-time flame temperature  $\sim 100$  K are observed for the heptane flame. The results are consistent with the assumption of negligible Soret effects often made in the literature concerning methane flames. The variables most sensitive to Soret diffusion tend to be the



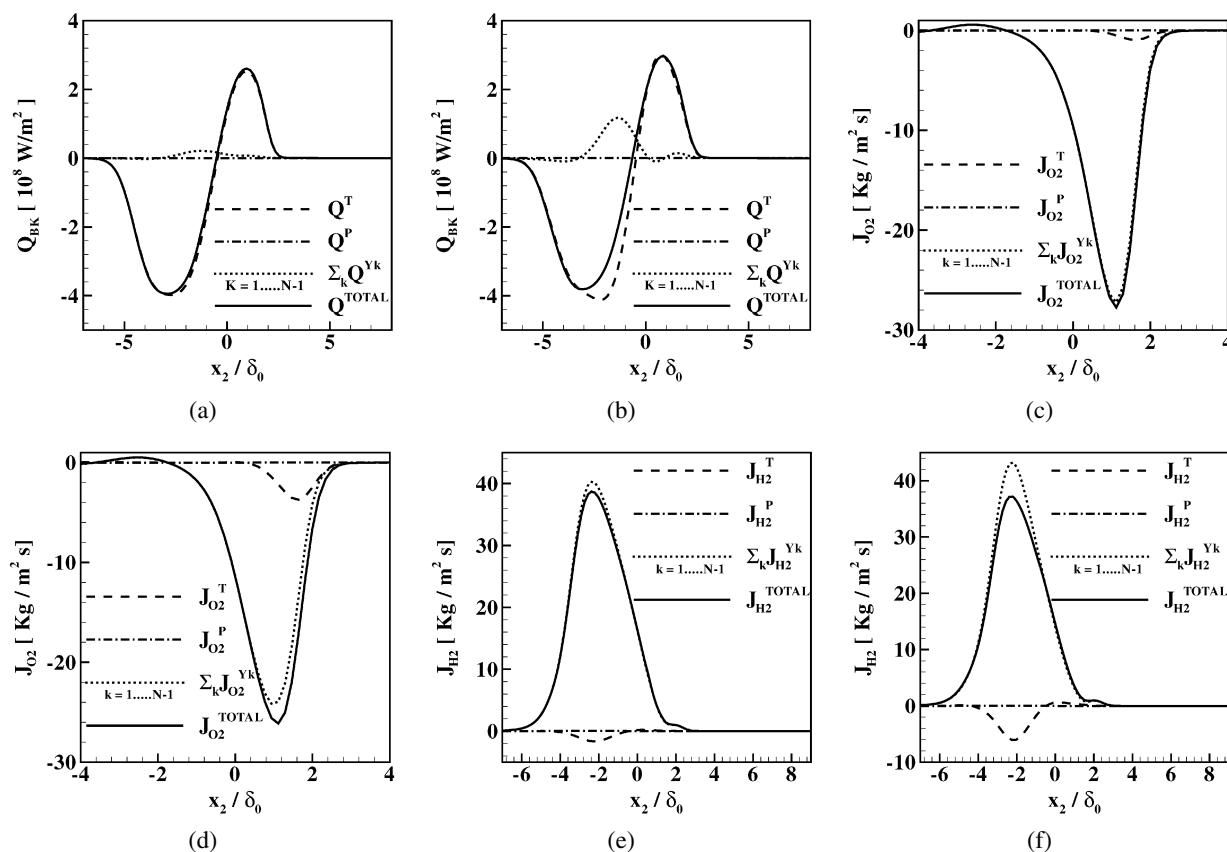


Fig. 8. Final time ( $t^* = 20$ ) heat and mass flux vector profiles for the base case  $H_2$ /air flame ( $T_0 = 700$  K,  $P_0 = 100$  atm): BK heat flux vector for the (a) FM and (b) KM model,  $O_2$  mass flux vector for the (c) FM and (d) KM model, and the  $H_2$  mass flux vector for the (e) FM and (f) KM model.

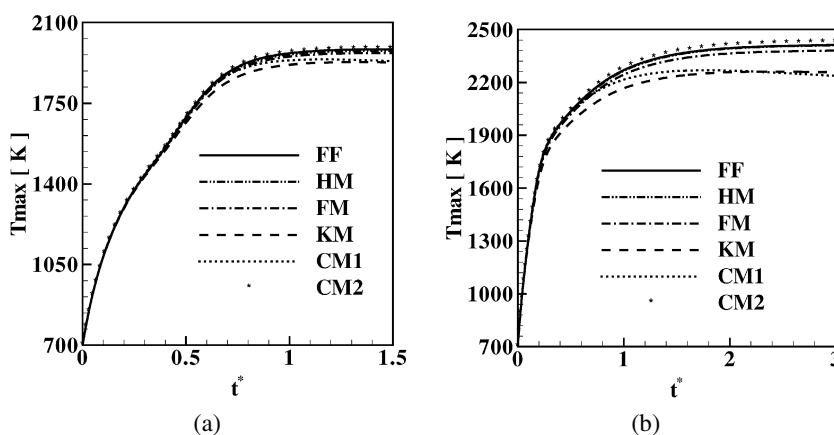


Fig. 9. Maximum flame temperature evolution for the base case ( $T_0 = 700$  K,  $P_0 = 35$  atm): (a)  $CH_4$ /air and (b)  $C_7H_{16}$ /air flames.

$NO_x$  mass fractions. These mass fraction profiles for methane are shown in Fig. 10 for  $NO$  and  $NO_2$  for each of the thermal-diffusion-factor models. In this case, the KM model actually results in the strongest deviations from the Fickian/Fourier cases with significant reductions in  $NO$  in particular. The remaining species concentrations are relatively unaffected by cross-diffusion for methane. Finally, the heptane flame is substantially more affected by cross-diffusion than the methane flame. Long-time mass fraction profiles for several species are presented for the base case

heptane reaction in Fig. 11. Both the FM and KM models result in significant variations in the maximum mass fractions for several of the species, including  $H$ ,  $H_2$ ,  $NO$ , and  $NO_2$ . These differences may be attributable to the overly simplified reduced kinetics mechanisms used in the above which lack some radicals important in detailed mechanisms. Nevertheless, use of reduced kinetics mechanisms is prevalent in the community and the effects of Soret and Dufour diffusion together with such mechanisms is of interest.

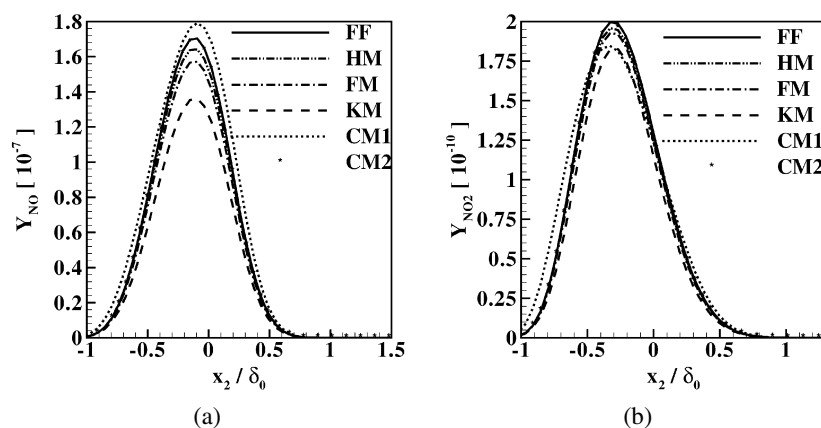


Fig. 10. Final time ( $t^* = 1.5$ )  $\text{NO}_x$  mass fraction profiles for the base case ( $T_0 = 700$  K,  $P_0 = 35$  atm)  $\text{CH}_4/\text{air}$  flames: (a) NO and (b)  $\text{NO}_2$ .

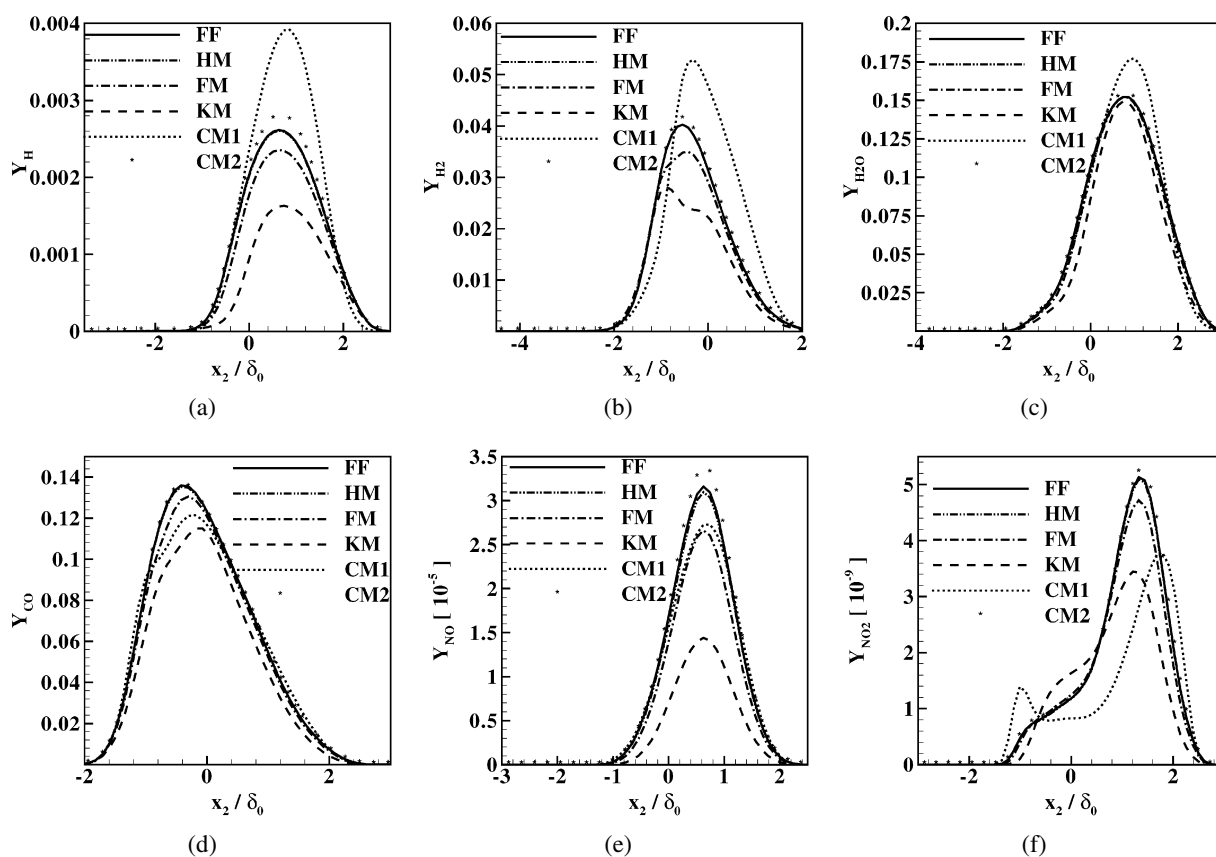


Fig. 11. Final time ( $t^* = 3$ ) mass fraction profiles for the base case ( $T_0 = 700$  K,  $P_0 = 35$  atm)  $\text{C}_7\text{H}_{16}/\text{air}$  flames: (a) H, (b)  $\text{H}_2$ , (c)  $\text{H}_2\text{O}$ , (d) CO, (e) NO, and (f)  $\text{NO}_2$ .

### 3.2.3. Effects of ambient pressure

The results presented thus far are for specific base case values of the ambient pressure. One of the more interesting questions that the present generalized formulation is capable of addressing concerns the effects of pressure on the relative impact of cross-diffusion on the various flames. Fig. 12 directly addresses this question through a presentation of the differences in the maximum flame temperature between each of the various thermal diffusion factor model predictions with those of the purely Fickian/Fourier diffusion model as a function of pressure. Each symbol

on the curves corresponds to the results of two entire simulations conducted at specific pressure values (i.e., results of the FF model and the model listed in the legends). Results are presented for the  $\text{H}_2/\text{air}$ ,  $\text{H}_2/\text{O}_2$ ,  $\text{CH}_4/\text{air}$ , and  $\text{C}_7\text{H}_{16}/\text{air}$  flames in Figs. 12a–12d, respectively. For all flames other than the methane flame increasing pressure is observed to increase the effects of cross-diffusion on the flame temperature. For all but the CM2 model (with unphysical constant thermal diffusion factors), cross-diffusion acts to decrease the flame temperature with respect to the FF model. These effects are largest for the hydrogen

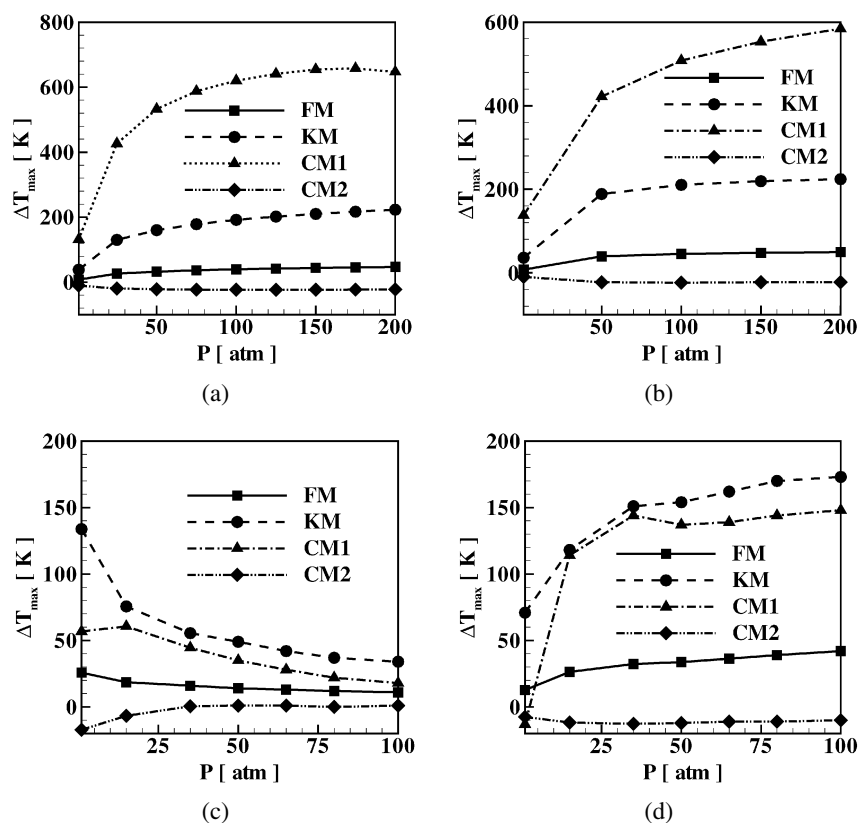


Fig. 12. Differences in the maximum flame temperature predicted by the Fickian/Fourier (FF) diffusion model from corresponding values predicted by the various thermal diffusion factor models as a function of the ambient pressure for: (a)  $\text{H}_2/\text{air}$ , (b)  $\text{H}_2/\text{O}_2$ , (c)  $\text{CH}_4/\text{air}$ , and (d)  $\text{C}_7\text{H}_{16}/\text{air}$  flames.

flames, but are substantial at large pressures for the heptane flame. In contrast, flame temperature alterations due to cross-diffusion actually decrease with increasing pressure for methane. This discrepancy is not readily explained as the overall effect of cross-diffusion is very complicated given the number of species involved in the reaction and their respective property variations. However, the trend is observed for all thermal-diffusion-factor models analyzed. It is not clear whether or not this trend would hold given a detailed (as opposed to reduced) kinetics model. Even the more conservative FM model predicts maximum flame temperature changes  $\sim 50$  K that can affect radical and pollutant species concentrations to a significant extent. The KM model predicts even larger variations  $\sim 150 \rightarrow 200$  K at high-pressures for flames other than methane with even larger potential for species concentration alterations.

#### 4. Conclusions

A generalized formulation for high-pressure laminar flame simulations has been developed and implemented for detailed  $\text{H}_2/\text{O}_2$  and  $\text{H}_2/\text{air}$  combustion, and reduced mechanisms describing  $\text{CH}_4/\text{air}$  and  $\text{C}_7\text{H}_{16}/\text{air}$  combustion. The formulation is based on the compressible Navier–Stokes equations cou-

pled with a real gas state equation and generalized heat and mass flux vectors derived from nonequilibrium thermodynamics and fluctuation theory. Accurate models based on the principle of corresponding states are employed for all mixture properties. Each of the kinetics mechanisms was chosen from the literature based on having pressure-dependent reaction steps and published comparisons with high-pressure data. In addition, several models previously presented in the literature for the thermal diffusion coefficient pairs related to Soret and Dufour cross-diffusion were implemented after comparing their predictions with available high-pressure (although relatively low-temperature) experimental data. The majority of the models were shown to agree qualitatively with the experimental data; however, no model predicted all of the data quantitatively. In general, those models capable of predicting hydrocarbon/hydrocarbon species pair data well fared more poorly with hydrocarbon/nonhydrocarbon species pairs, and vice versa. Each of the models was then implemented into the general flame code for one-dimensional laminar diffusion flames that were simulated across a large range of ambient pressures.

The ultimate impact of cross-diffusion varied substantially as a function of the model used to predict the thermal diffusion coefficient pairs. Several of the models were argued to be physically implausi-

ble at the large temperatures present within the flame zones. Two models were identified as being the most physically plausible: the “Kempers model” (denoted KM) [55] and the “Shukla and Firoozabadi model” (denoted FM) [50]. The FM model resulted in the more conservative predictions with respect to purely Fourier/Fickian diffusion modeling. However, a need was found for experimental data for thermal diffusion coefficients at both high pressure and high temperature needed to further evaluate the accuracy of thermal diffusion modeling in high-pressure flames (although such measurements are expected to be very difficult due to the onset of chemical reactions at high temperatures). Nevertheless, for all flames other than the methane flame, significant alterations to both the flame temperature and species concentrations were observed due to cross-diffusion for nearly all of the models. These alterations are particularly apparent in  $\text{NO}_x$  concentrations, and increase with increasing pressure. While not conclusive, the results suggest that proper multicomponent diffusion modeling, including Soret and Dufour cross-diffusion, be included for high-fidelity simulations of laminar diffusion flames. These effects become particularly important when accurate predictions of pollutant species are required, and/or for large pressures associated with modern combustion devices. The results of the study are, however, limited to laminar flames. Further research is required before the ultimate impact of multicomponent and cross-diffusion on turbulent reacting flows can be comprehensively addressed.

## Acknowledgments

The authors thank Dr. John C. Hewson of Sandia National Laboratories for providing the high-pressure reaction kinetics for the hydrocarbon flames. Drs. Daniel E. Rosner and Abbas Firoozabadhi are also thanked for discussions concerning various thermal diffusion coefficient models and their implementation. This work was partially funded by National Science Foundation Grant CTS-9983762.

## References

- [1] R. Reid, J. Prausnitz, B. Poling, *The Properties of Gases and Liquids*, McGraw-Hill, Boston, MA, 1987.
- [2] T. Kamimoto, H. Kobayashi, *Prog. Energy Combust. Sci.* 17 (1991) 163–189.
- [3] R. Reitz, C. Rutland, *Prog. Energy Combust. Sci.* 21 (1995) 173–196.
- [4] R. Marcer, P. Le Cottier, H. Chaves, B. Argueyrolles, C. Habchi, B. Barbeau, SAE Paper 2000-01-2932.
- [5] G. Bianchi, P. Pelloni, F. Corcione, L. Allocca, F. Lupino, *J. Eng. Gas Turbines Power* 123 (2001) 419–427.
- [6] E. de Villiers, A. Gosman, H. Weller, SAE Paper 2004-01-0100.
- [7] A. Lefebvre, *Gas Turbine Combustion*, Taylor & Francis, Ann Arbor, MI, 1998.
- [8] S. Palle, C. Nolan, R. Miller, *Phys. Fluids* 17 (2005) 103601-1–103601-19.
- [9] S. Palle, Ph.D. dissertation, Department of Mechanical Engineering, Clemson University, December 2006.
- [10] R. Hilbert, F. Tap, H. El-Rabii, D. Thevenin, *Prog. Energy Combust. Sci.* 30 (2004) 61–117.
- [11] V. Gopalakrishnan, J. Abraham, *Combust. Flame* 136 (2004) 557–566.
- [12] S. Chapman, T. Cowling, *The Mathematical Theory of Non-Uniform Gases*, Cambridge Univ. Press, Cambridge, 1970.
- [13] A. Ern, V. Giovangigli, *Combust. Sci. Technol.* 149 (1999) 157–181.
- [14] C. Curtiss, R. Bird, *Ind. Eng. Chem. Res.* 38 (1999) 2515–2522.
- [15] J. Charentenay, A. Ern, *Combust. Theory Model.* 6 (2002) 439–462.
- [16] A. Ern, V. Giovangigli, *J. Comput. Phys.* 120 (1995) 105–116.
- [17] M. Desilets, P. Proulx, G. Soucy, *Int. J. Heat Mass Transfer* 40 (18) (1997) 4273–4278.
- [18] P. Paul, J. Warnatz, in: *Proceedings of the 27rd Symposium (International) on Combustion*, 1998, pp. 495–504.
- [19] F. Liu, O. Gulder, *Combust. Flame* 143 (2005) 264–281.
- [20] B. Greenberg, *Combust. Sci. Technol.* 24 (1980) 83–88.
- [21] P. Garcia-Ybarra, C. Nicoli, P. Clavin, *Combust. Sci. Technol.* 42 (1984) 87–109.
- [22] A. Ern, V. Giovangigli, *Combust. Theory Model.* 2 (1998) 349–372.
- [23] D. Rosner, R. Israel, B. La Mantia, *Combust. Flame* 123 (2000) 547–560.
- [24] R. Dakhalia, V. Giovangigli, D. Rosner, *Combust. Theory Model.* 6 (2002) 1–17.
- [25] H. Guo, F. Liu, G. Smallwood, O. Gulder, *Int. J. Comput. Fluid Dynam.* 18 (2) (2004) 139–151.
- [26] A. Briones, I. Puri, S. Aggarwal, *Combust. Flame* 140 (2005) 46–59.
- [27] S. De Groot, P. Mazur, *Non-Equilibrium Thermodynamics*, Dover, New York, 1984.
- [28] J. Keizer, *Statistical Thermodynamics of Nonequilibrium Processes*, Springer-Verlag, New York, 1987.
- [29] K. Harstad, J. Bellan, *Int. J. Multiphase Flow* (2000) 1675–1706.
- [30] K. Harstad, J. Bellan, *J. Chem. Phys.* 120 (12) (2004) 5664–5673.
- [31] K. Harstad, R. Miller, J. Bellan, *AIChE J.* 43 (6) (1997) 1605–1610.
- [32] K. Harstad, J. Bellan, *Int. J. Heat Mass Transfer* 41 (1998) 3537–3550.
- [33] K. Harstad, J. Bellan, *Int. J. Heat Mass Transfer* 41 (1998) 3551–3558.
- [34] K. Harstad, J. Bellan, *Int. J. Heat Mass Transfer* 42 (1999) 961–970.
- [35] R. Miller, K. Harstad, J. Bellan, *J. Fluid Mech.* 436 (2001) 1–39.
- [36] N. Okong’o, J. Bellan, *J. Fluid Mech.* 464 (2002) 1–34.



- [37] N. Okong'o, K. Harstad, J. Bellan, *AIAA J.* 40 (5) (2002) 914–926.
- [38] J. Bellan, *Prog. Energy Combust. Sci.* 26 (2000) 329–366.
- [39] J. Bellan, *Combust. Sci. Technol.* 178 (2006) 253–281.
- [40] E. Curtis, P. Farrell, *Combust. Flame* 90 (1992) 85–102.
- [41] R. Miller, *Phys. Fluids* 12 (8) (2000) 2020–2032.
- [42] H. Lou, R. Miller, *Phys. Fluids* 13 (11) (2001) 3386–3399.
- [43] H. Lou, Ph.D. dissertation, Department of Mechanical Engineering, Clemson University, December 2002.
- [44] H. Lou, R. Miller, *Phys. Fluids* 16 (5) (2004) 1423–1438.
- [45] C. Wilke, *Chem. Eng. Prog.* 46 (1950) 95–104.
- [46] J. Ramshaw, *J. Nonequilib. Thermodynam.* 15 (1990) 295–300.
- [47] National Institute of Standards and Technology Webbook, <http://webbook.nist.gov/chemistry/fluid/>.
- [48] K. Haugen, A. Firoozabadi, *J. Chem. Phys.* 122 (2005) 014516.
- [49] J. Platen, *J. Appl. Mech.* 73 (2006) 5–15.
- [50] K. Shukla, A. Firoozabadhi, *Ind. Eng. Chem. Res.* 37 (1998) 3331–3342.
- [51] M. Gonzalez-Bagnoli, A. Shapiro, E. Stenby, *Phil. Mag.* 83 (17–18) (2003) 2171–2183.
- [52] A. Firoozabadi, K. Ghorayeb, K. Shukla, *AIChE J.* 46 (5) (2000) 892–900.
- [53] A. Leahy-Dios, M. Bou-Ali, J. Platten, A. Firoozabadi, *J. Chem. Phys.* 122 (2005) 234502.
- [54] R. Hasse, *Thermodynamics of Irreversible Processes*, Addison–Wesley, Reading, MA, 1963.
- [55] L. Kempers, *J. Chem. Phys.* 90 (1989) 6541–6548.
- [56] S. Pan, C. Jiang, Y. Yan, M. Kawaji, M. Saghir, *J. Non-Equilib. Thermodynam.* 31 (2006) 47–71.
- [57] C. Sohn, S. Chung, *Combust. Flame* 121 (2000) 288–300.
- [58] S. Chung, S. Lee, F. Mauss, N. Peters, in: N. Peters, B. Rogg (Eds.), *Reduced Kinetic Mechanisms Applications in Combustion Systems*, in: *Lecture Notes in Physics*, vol. 15, Springer-Verlag, Berlin, 1993, pp. 308–328.
- [59] J. Hewson, M. Bolig, *Proc. Combust. Inst.* 26 (1996) 2171–2179.
- [60] M. Bolig, H. Pitsch, J. Hewson, K. Sheshadri, *Proc. Combust. Inst.* 26 (1996) 729–737.
- [61] C. Kennedy, M. Carpenter, *Appl. Numer. Math.* 14 (1994) 397–433.
- [62] T. Poinso, S. Lele, *J. Comput. Phys.* 101 (1992) 104–129.
- [63] S. Takahashi, M. Hongo, *J. Chem. Eng. Jpn.* 15 (1982) 57–59.